THE UNIVERSITY OF TULSA

THE GRADUATE SCHOOL

EXPERIMENTS, CFD SIMULATION AND MODELING OF ESP PERFORMANCE UNDER VISCOUS FLUID FLOW CONDITIONS

By
Jiecheng Zhang

A thesis submitted in partial fulfillment of

the requirements for the degree of Master of Science

in the Discipline of Petroleum Engineering

The Graduate School

The University of Tulsa

2017

THE UNIVERSITY OF TULSA

THE GRADUATE SCHOOL

EXPERIMENTS, CFD SIMULATION AND MODELING OF ESP PERFORMANCE UNDER VISCOUS FLUID FLOW CONDITIONS

By
Jiecheng Zhang

A THESIS

APPROVED FOR THE DISCIPLINE OF

PETROLEUM ENGINEERING

By Thesis Committee

Hong-Quan Zhang, Chair
Mauricio Prado
Ruben Cuamatzi Melendez

COPYRIGHT STATEMENT

ABSTRACT

Jiecheng Zhang (Master of Science in Petroleum Engineering)

Experiments, CFD Simulation and Modeling of ESP Performance under Viscous Fluid Flow Conditions

Directed by Dr. Hong-Quan Zhang

95 pp., Chapter 5: Conclusions and Recommendations

(249 words)

A 3-inch vertical closed liquid flow loop is built to test a 14-stage radial type electrical submersible pump (ESP) under viscous fluid flow conditions. A pipe-in-pipe heat exchanger is constructed to control the temperature and a pipe viscometer is employed to measure the fluid viscosity. A mineral oil is used as the working fluid. The ESP hydraulic heads are measured with oil viscosities of 37, 54, 74, 80, 98, and 107 cP at 2,400 rpm and with oil viscosities of 45, 54, 67, 74, and 82 cP at 3,500 rpm. The ESP head curves deteriorate with fluid viscosity increase.

Three-dimensional computational fluid dynamics (CFD) is implemented to study the viscous influence on ESP and help flow loop design. CFD simulations are carried out to obtain the ESP head curves at 1, 3, 5, 10, 30, 50, 100, 300, 500, and 1,000 cP. Compared with experimental measurements, the head predicted by CFD with viscous fluid is higher.

A mechanistic model is developed to predict ESP hydraulic head based on Euler's equation. A flow rate at the best match point (BMP) is utilized to find the effective velocity at the ESP impeller outlet so that the recirculation is considered. Friction losses and the losses due to flow direction change are also taken into account. The mechanistic model predictions of ESP head are validated with two types of ESP, one is a radial type tested in this study and the other one is a

mixed type. The prediction errors are within ±10%.

ACKNOWLEDGEMENTS

I would like to thank my advisor, Dr. Hong-Quan Zhang, for letting me be his master's student and for allowing me to work as a Research Assistant for the Tulsa University Artificial Lift Projects (TUALP). I could not accomplish my master's study without his guidance, encouragement, and support. His stringent attitude and tireless devotion to academic excellence lead me into becoming a qualified researcher, not only during the past two and half years but also in the future.

I would like to acknowledge the TUALP team for offering generous help whenever needed. Many thanks to the Project Engineer, Mr. Bryan Sams, for his technical assistance during the flow loop construction and for his safety instruction. I also thank the Project Assistant, Mrs. Donna Trankley, for her professional management and thesis proofreading. I extend my thanks to Dr. Jianjun Zhu for his help on experiment and thesis revision. I thank to Haiwen Zhu for the discussions of facility design and help during the flow loop construction. I wish to thank Hattan Banjar for sharing his research ideas and thank Fahad Al-Mudairis for bringing joys into the team.

I am also grateful to Tonghui Zhu, Tong Liu, Dawei Xu, and Yuchen Ji for helping me build up the flow loop and Dishi Zheng for helping me collect experimental data. I could not finish the experimental study without their assistance.

I would like to express my sincere appreciation to Dr. Mauricio Prado and Dr. Ruben Cuamatzi Melendez for serving on my thesis committee, reviewing my thesis, and offering their constructive comments.

At last, I want to extend my deepest gratitude to my parents, Dr. Shimin Zhang and Mrs.

Xingmei Chen, whose unconditional love and encouragement have always helped me face challenges during my academic pursuit.

TABLE OF CONTENTS

LIST OF FIGURES

LIST OF TABLES

INTRODUCTION

ESP is an artificial lift used in oil industry. It has become more and more popular in offshore production to produce medium-to-heavy oils (Amaral et al., 2009). The ESP can lift high liquid volume from the subsea. Therefore, large production systems use the ESP as a boosting pump.

The ESP consists of multiple stages of centrifugal pumps and each stage comprises a rotating impeller and a stationary diffuser. The ESP motor transforms electric power into mechanical energy and drives the ESP at a certain rotational speed. With hydrocarbon fluids boosted by the rotating impellers in an ESP, the shaft energy from the motor is converted into the kinetic energy of liquids. Guided by the diffuser, the fluids from upstream impellers change flow direction and the kinetic energy is transformed into hydraulic pressure energy.

A production system design is based on the nodal analysis. Usually, the node is set at the well bottom hole. In this case, according to reservoir and perforation conditions, an inflow performance relationship (IPR) is applied which relates the flow rate to the pressure at the well bottom hole. Meanwhile, an outflow performance relationship (OPR) is formulated based on well, artificial lift equipment, and surface facility conditions. Once an ESP is taken into consideration for a production system, an accurate prediction of ESP hydraulic performance (boosting pressure, hydraulic efficiency, etc.) is required. However, only the single-phase water *H*-*Q* performance curves are provided by the manufacturers. Since the oil viscosity can dramatically influence an ESP performance, the ESP pressure increment degrades significantly with the viscosity increase. Moreover, the crude oil viscosity varies due to different chemical compositions and local PVT

conditions, which must be considered when designing a reliable production system involving an ESP.

So far, four methodologies have been employed to analyze viscous effects on ESP hydraulic performance in literature. The first one is experimentation, by which the researchers can test an ESP under different flow conditions, such as changing rotational speeds, flow rates, and oil viscosities. With the experimental testing results, a database can be set up. In production system design, the field operation scenario may be covered by the cases that have been stored in the database. Thus, an OPR can be obtained for the specific production design. This approach, as it might be the easiest way to consider the viscous effect, does provide good accuracy to estimate ESP boosting pressure under viscous fluid flow conditions. However, the crude oils usually have a wide viscosity range. Thus, it is impossible to test the ESP performance in terms of the boosting pressure and hydraulic efficiency for all scenarios.

The second method is the correlation, which is the empirical relationship found from experiments without theory derivation. Most of the previous studies are correlations due to the complicated flow structure in ESP. However, correlations might not work all the time.

The third method is the CFD, the numerical simulation to study fluid flow governed by the Navier-Stokes equations. CFD helps understand the fluid behaviors inside the complicated geometries such as ESPs, but it also needs professional backgrounds of fluid mechanics. Furthermore, the fluid domains in impellers and diffusers of an ESP are twisted and highly curved. To conduct a successful CFD simulation, a proper mesh with high-quality grids must be created. Also, a series of numerical schemes, including boundary conditions and discretization algorithms for time and space domain, need to be applied. With the above setup, the CFD simulation requires longer computational time as the mesh grid number increases. In order to obtain an ESP *H*-*Q* curve

under a specific working condition, at least 10 points need to be simulated, which is highly time-consuming.

The last method to estimate ESP head under viscous fluid flow conditions is mechanistic modeling. Unlike numerical solutions, the mechanistic model predicts ESP performance quickly and reliably, which can be used for a variety of field applications.

In this study, CFD simulation is used to help understand ESP's internal flow structures. The CFD simulation results also support the design of experimental flow loop. The instruments, such as pressure transmitters, temperature transmitters, and flow meters, are selected based on the measurement ranges estimated before the tests being conducted. A closed 3-inch diameter flow loop with a vertical layout is constructed to test ESP performance with viscous oils. A mechanistic model is developed to predict the ESP head under viscous fluid flow conditions. The model is validated with experimental results.

CHAPTER 1

LITERATURE REVIEW

This chapter summarizes previous experimental and modeling studies of viscous effects on ESP performance.

1.1 Ippen

Ippen (1946) conducted over 220 tests for oil viscosities up to 10,000 Saybolt universal second (SSU) with four different centrifugal pumps. The pump head, capacity, and input-power changes with viscous fluids were also measured at different pump speeds. This was the first systematic study of centrifugal pump performance change with viscosity increase under the controlled laboratory flow conditions. Three types of oils were used including heavy oil, light oil, and thin oil. Thin oil is a mixture of light oil and fuel oil.

To analyze the hydraulic performance of centrifugal pumps, several important geometric variables were considered, including pipe dimensions and shape, pump inlet design, and the dimensions of impeller and diffuser.

Four kinds of pressure losses inside a rotating centrifugal pump were defined, hydraulic loss, disk friction, ring loss, and miscellaneous loss. The ring loss was included since the shaft torque loss was directly related to fluid viscosity due to the tangential shear induced by the rotation of the pump ring inside the stationary housing ring.

Three ratios were introduced to describe the centrifugal pump performance under viscous fluid flow, including the ratio of oil head to water head (H_o/H_w), the efficiency loss ((100-e)/100),

and the ratio of oil power input to water power input with a correction of oil specific gravity ($BHP_o/(s_o \cdot BHP_w)$).

These parameters were plotted against a Reynolds number, which was defined as

$$R_D = 2620 \frac{N{d_2}^2}{\nu \cdot 10^5} \tag{1.1}$$

where N is the rotational speed of the impeller in rpm, d_2 is the impeller diameter in ft, and ν is the kinematic viscosity in cSt.

As for the viscosity effect on pump performance, pump hydraulic head decreases while power input and efficiency losses increase with increasing fluid viscosity. Therefore, with the Reynolds number decrease, H_o/H_w increases while (100-e)/100 and $BHP_o/(s_o \cdot BHP_w)$ decreases as shown in Figure 1.1 for Pump IL 1 and in Figure 1.2 for Pump IL 2.

Ippen tried to explain the principle behind the results. However, the results obtained for Pump IL 1 and IL 2 cannot be extended to other centrifugal pumps.

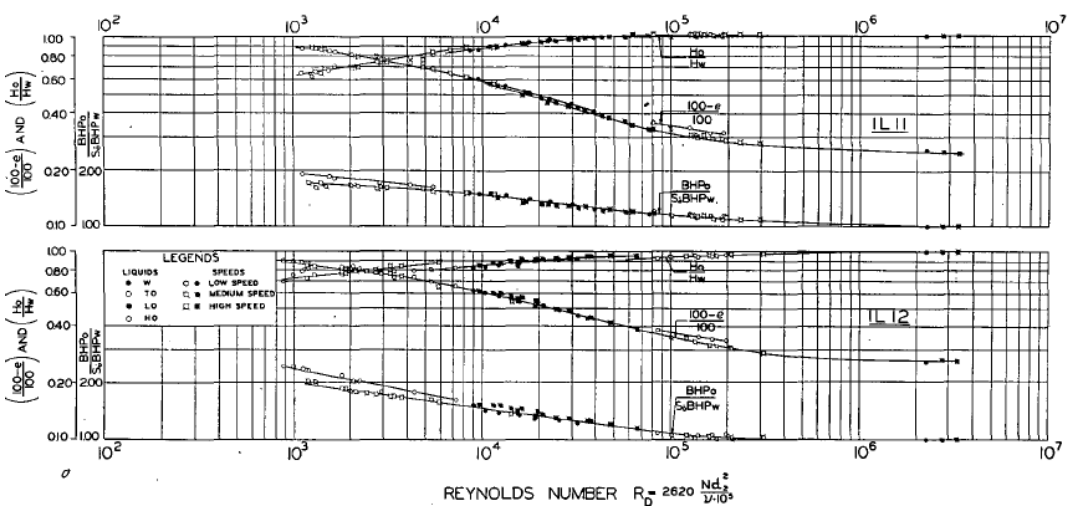

Figure 1.1 Results Plotted against R_D for Pump IL 1

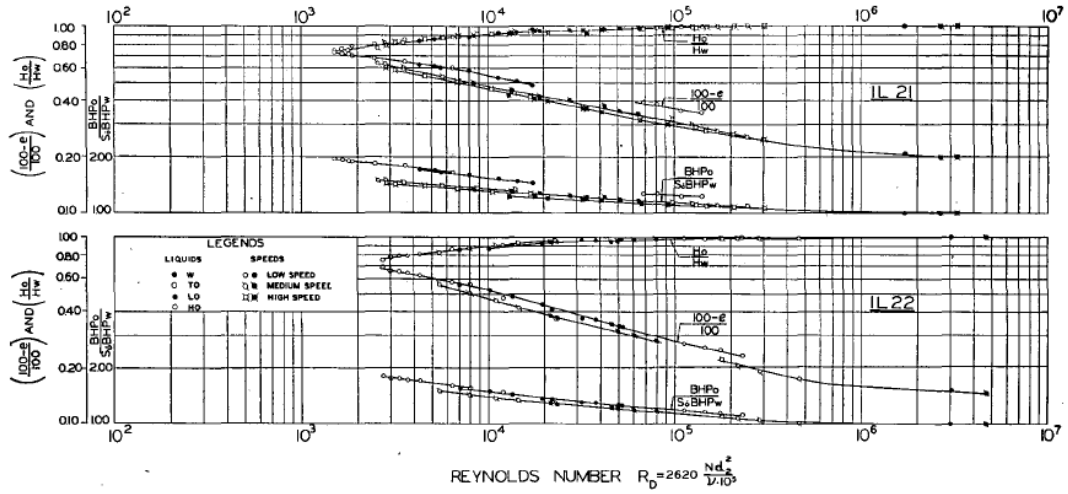

Figure 1.2 Results Plotted against R_D for Pump IL 2

1.2 Stepanoff

Stepanoff (1946) conducted experiments with fluid viscosities ranging from 1 to 2,000 cSt. A specific speed, N_s, was defined to identify the impeller operated at the best efficiency point (BEP) as

$$N_s = \frac{\sqrt{q_{bep}}N}{H_{bep}^{3/4}g^{3/4}} \tag{1.2}$$

where q_{bep} is the pump capacity at the BEP in gpm, N is the impeller rotational speed in rpm, H_{bep} is the pump head at the BEP in ft, and g is the gravity acceleration in ft/s^2.

The specific speed was expected to remain the same no matter what kind of fluid is pumped, corresponding to a constant rotational speed of the impeller. Based on the results from water to viscous fluid, an equation can be written as

$$\frac{\sqrt{q_{bep}^{water}}N}{\left(H_{bep}^{water}\right)^{3/4}} = \frac{\sqrt{q_{bep}^{vis}}N}{\left(H_{bep}^{vis}\right)^{3/4}} \tag{1.3}$$

where q_{bep}^{water} is the water flow rate at the BEP in gpm, q_{bep}^{vis} is the viscous fluid flow rate at the BEP in gpm, H_{bep}^{water} is the water head at the BEP in ft, H_{bep}^{vis} is the viscous fluid head at the BEP in ft, and N is the impeller rotational speed in rpm.

A new relation is established at the constant rotational speed as

$$\frac{q_{bep}^{vis}}{q_{bep}^{water}} = \left(\frac{H_{bep}^{vis}}{H_{bep}^{water}}\right)^{1.5} \tag{1.4}$$

The flow rate and head correction factors are defined in Eq. (1.5) and (1.6) respectively:

$$F_Q = \frac{q_{bep}^{vis}}{q_{bep}^{water}} \tag{1.5}$$

$$F_H = \frac{H_{bep}^{vis}}{H_{bep}^{water}} \tag{1.6}$$

Hence, the Eq. (1.4) can be rewritten as

$$F_Q = (F_H)^{1.5} \tag{1.7}$$

As Eq. (1.7) indicates, either the flow rate or head correction factor can be obtained by knowing one of them if the water performance is given, which provides a quick approach to calculate the centrifugal pump performance under viscous fluid flow conditions.

A new Reynolds Number, namely Stepanoff Reynolds Number, is defined as

$$R_{Stepanoff} = 6.0345 \frac{N q_{bep}^{vis}}{\sqrt{H_{bep}^{water}}\, v} \tag{1.8}$$

where N is the rotational speed in rpm, q_{bep}^{vis} is the viscous fluid flow rate at the BEP in bpd, H_{bep}^{water} is the water head at the BEP in ft, and v is the liquid kinematic viscosity in cSt.

The hydraulic efficiency, pump head factor, and flow capacity factor were plotted against the Stepanoff Reynolds Number as shown in Figure 1.3. In order to use the diagram, an initial

guess is needed for the viscous fluid flow rate. Then the pump head and flow capacity factor can be read from the chart corresponding to the specific Stepanoff Reynolds Number. Using the capacity factor, a new viscous fluid flow rate can be found. Several iterations are needed until the convergence is achieved. This correlation is based on the tested pumps, which means it might not work if the pump is different.

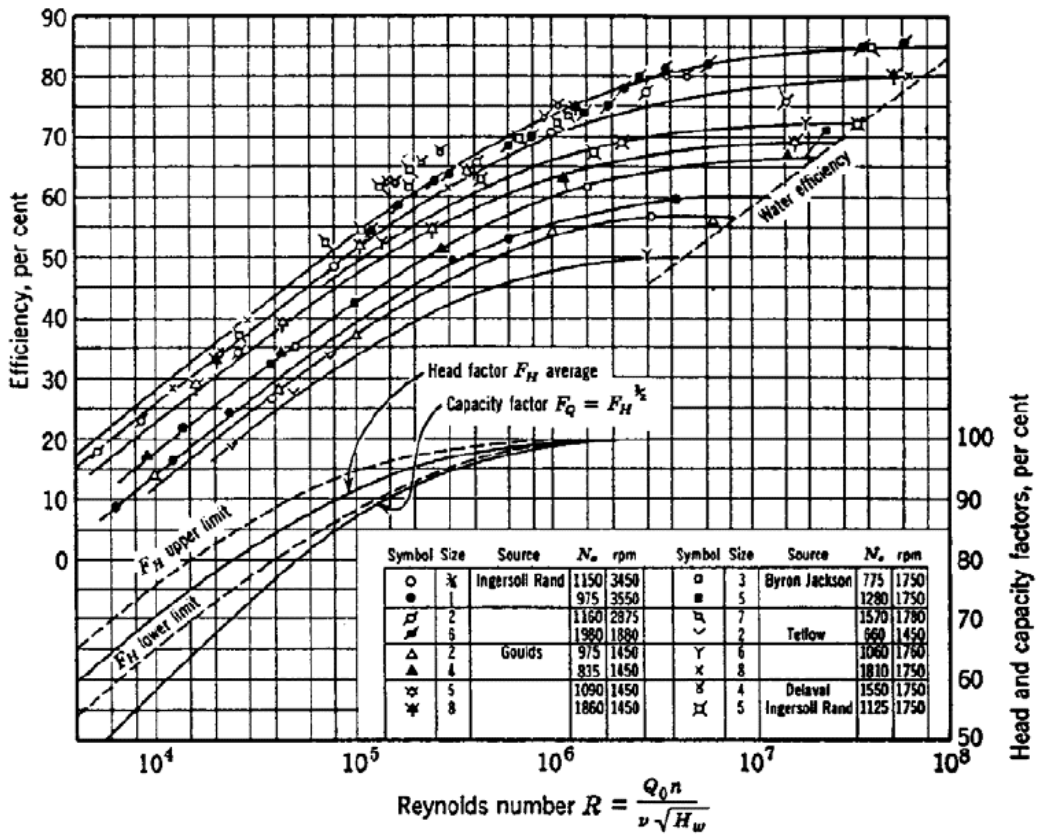

Figure 1.3 Head, Capacity, and Efficiency Factors for Viscous Fluid at BEP

1.3 Hydraulic Institute

Hydraulic Institute (1955) proposed a new method for estimating the centrifugal pump performance with the viscous fluid flow if the water performance curve is given. Three correction factors are defined as

$$C_Q = q_{vis}/q_w \tag{1.9}$$

$$C_H = H_{vis}/H_w \tag{1.10}$$

$$C_\eta = \eta_{vis}/\eta_w \tag{1.11}$$

where C_Q is the correction factor of flow rate, C_H is the correction factor of head, C_η is the correction factor of efficiency, q_{vis} and q_w are the flow rates with viscous fluid and water flow, H_{vis} and H_w are the heads with viscous fluid and water flow, η_{vis} and η_w are the efficiencies with viscous fluid and water flow, respectively.

With the dimensionless groups, the correction curves were summarized in Figure 1.6 and Figure 1.7. Figure 1.6 was based on 1 inch and smaller pumps while Figure 1.7 was obtained using 2 to 8 inches pumps.

Although the correction factors proposed by Hydraulic Institute are valid for a broad application range, experimental tests are still recommended for accuracy results.

A further improvement on correction factors was conducted by Hydraulic Institute (2004) to better correlate centrifugal pump performance with viscous fluid flow by introducing a parameter B defined as

$$B = K\left[\frac{(V_{vis})^{0.50}(H_{BEP-W})^{0.0625}}{(Q_{BEP-W})^{0.375}(N)^{0.25}}\right] \tag{1.12}$$

where K is a constant as 26.5, V_{vis} is the kinematic viscosity in cSt, H_{BEP-W} is the water head per stage at the BEP in ft, Q_{BEP-W} is the water flow rate at the BEP in gpm, and N is the pump shaft speed in rpm.

The improved correction curves are shown in Figure 1.4 and Figure 1.5, where the procedure was simplified but the concept behind remained the same.

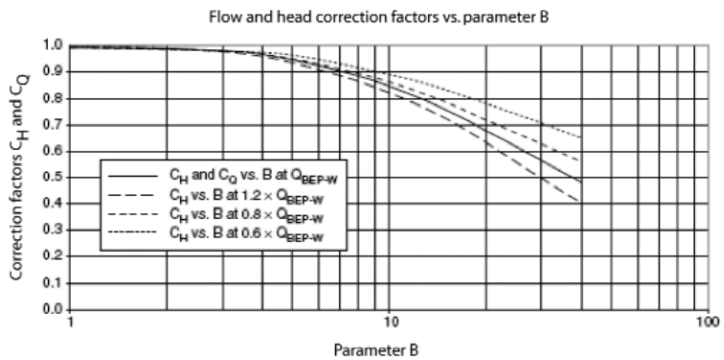

Figure 1.4 C_H and C_Q as Function of Parameter B

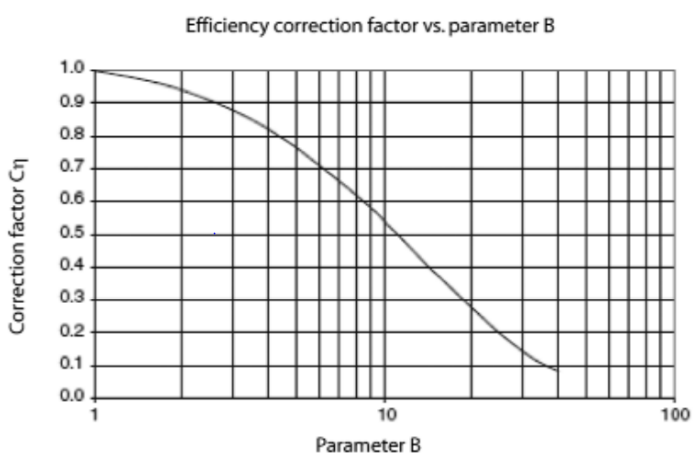

Figure 1.5 C_η as Function of Parameter B

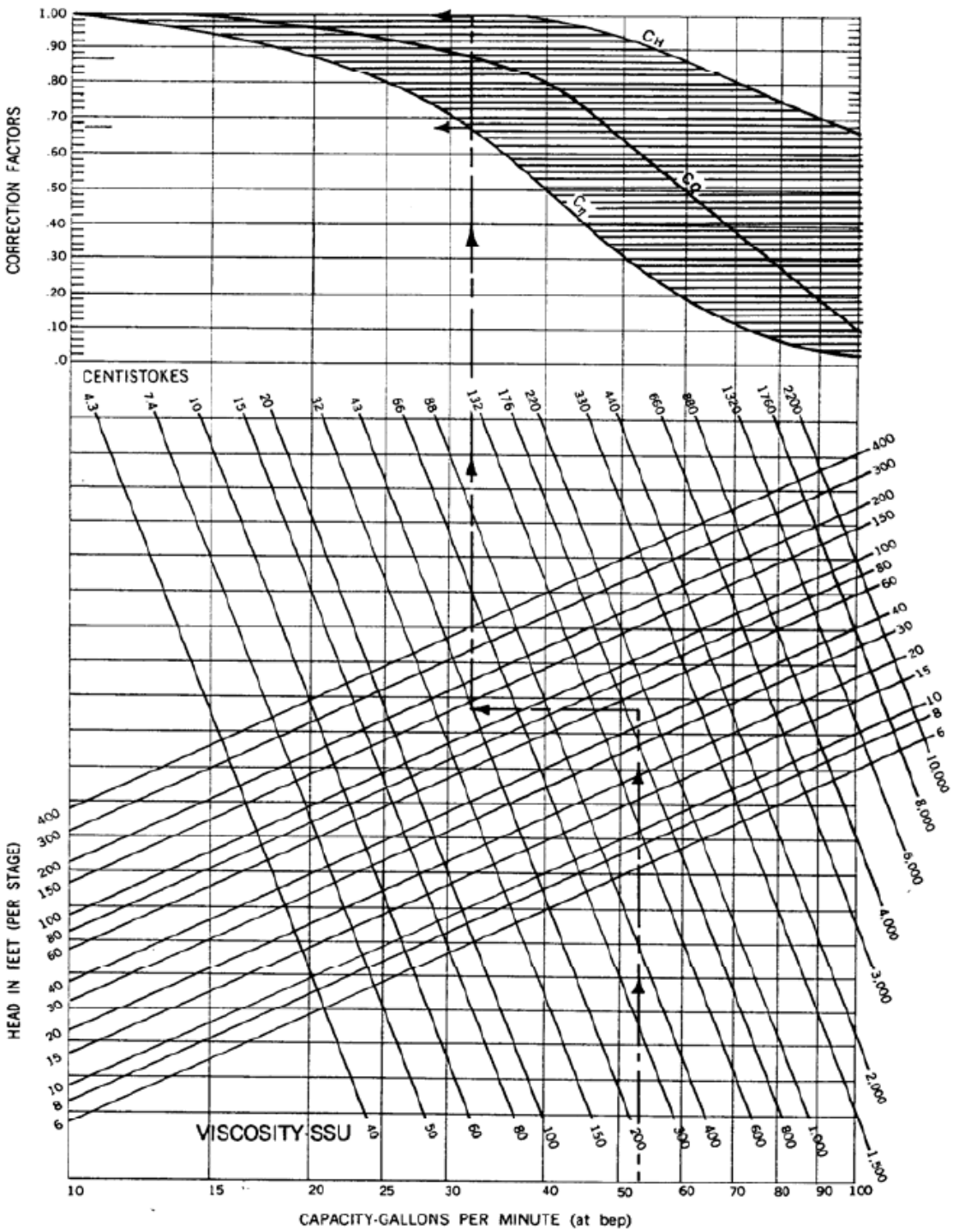

Figure 1.6 Performance Correction Chart for Viscous Liquids (1 Inch and Smaller Pumps)

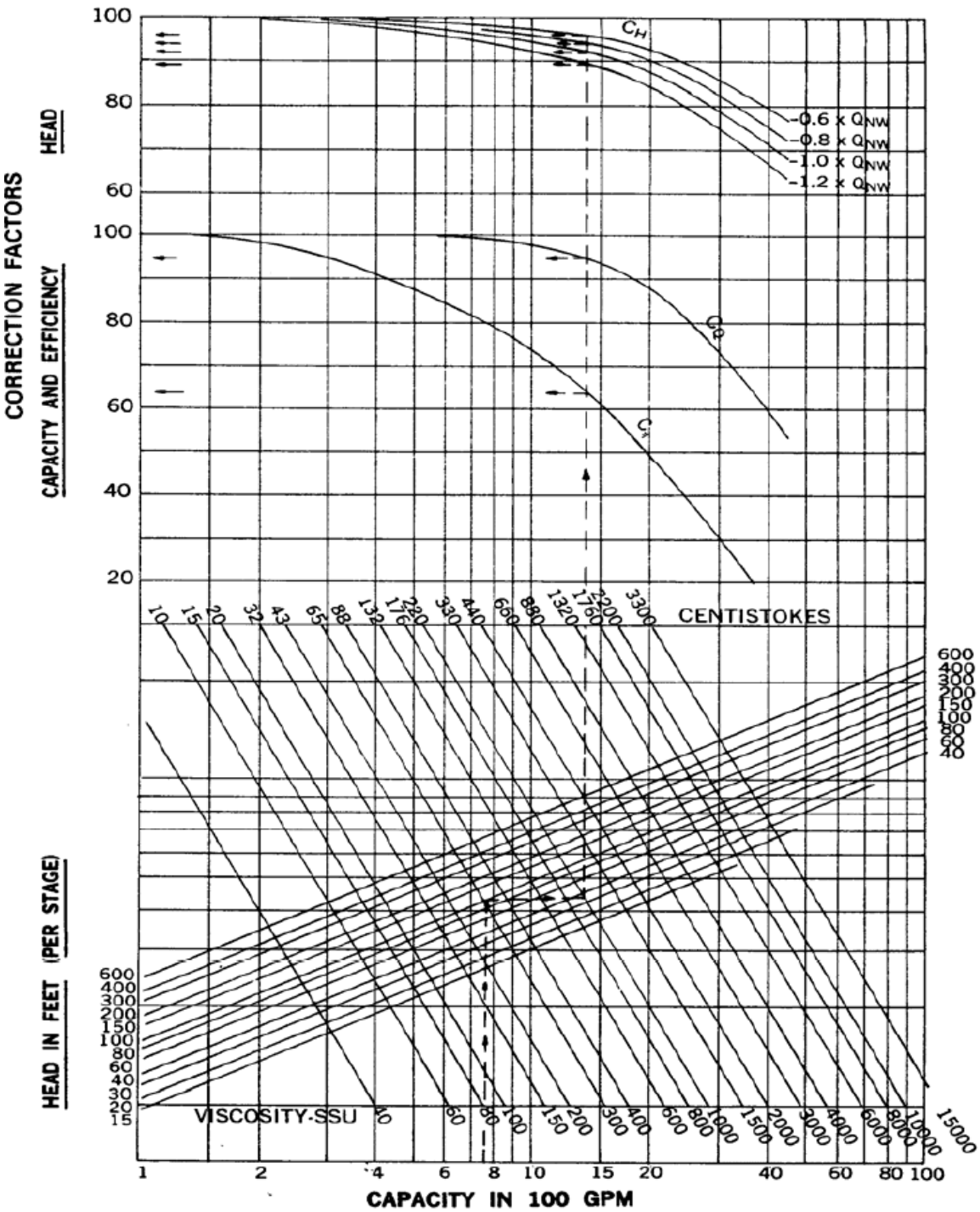

Figure 1.7 Performance Correction Chart for Viscous Liquids (2 to 8 Inches Pumps)

1.4 Hole

Hole (1994) generated calculation equations from Hydraulic Institute charts based on a regression analysis. The flow rate and head at the BEP should be given before applying the formulae to compute centrifugal pump performance under viscous fluid flow.

First, a term named pseudocapacity is defined as

$$P = 1.95v^{0.5}(0.04739H^{0.25746}Q^{0.5})^{-0.5} \tag{1.13}$$

where v is the fluid kinematic viscosity in cSt, H is the water head at the BEP in ft, and Q is the water flow rate at the BEP in gpm. Then, the correction factor is calculated by

$$C_x = D_{x1} + D_{x2}P + D_{x3}P^2 + D_{x4}P^3 + D_{x5}P^4 + D_{x6}P^5 \tag{1.14}$$

where C_x is the correspondent correction factor and D_{xn} is the correspondent polynomial coefficient listed in Table 1.1.

Table 1.1 Polynomical Coefficients

	D_{x1}	D_{x2}	D_{x3}	D_{x4}	D_{x5}	D_{x6}
C_η	1.0522	-3.5120E-02	-9.0394E-04	2.2218E-04	-1.1986E-05	1.9895E-07
C_Q	0.9873	9.0190E-03	-1.6233E-03	7.7233E-05	-2.0528E-06	2.1009E-08
$C_{H0.6}$	1.0103	-4.6061E-03	2.4091E-04	-1.6912E-05	3.2459E-07	-1.6611E-09
$C_{H0.8}$	1.0167	-8.3641E-03	5.1288E-04	-2.9941E-05	6.1644E-07	-4.0487E-09
$C_{H1.0}$	1.0045	-2.6640E-03	-6.8292E-04	4.9706E-05	-1.6522E-06	1.9172E-08
$C_{H1.2}$	1.0175	-7.8654E-03	-5.6018E-04	5.4967E-05	-1.9035E-06	2.1615E-08

In Table 1.1, the head correction factor depends on the flow rate so four flow rates, including 60%, 80%, 100%, and 120% of the water flow rate at the BEP, are used to form head performance curve under viscous fluid flow conditions.

The correction factors calculated by this method are within 1.0% of those found in the Hydraulic Institute chart. Therefore, it is convenient to apply these formulae to compare the mechanistic model prediction and Hydraulic Institute correction factors predictions.

1.5 Amaral et al.

Amaral et al. (2007) conducted an experimental study on two centrifugal pumps using water and clear glycerin. One pump is a semi-axial Schlumberger-Reda GN-7000/540 ESP with three impellers and the other is a two-impeller conventional radial pump. For GN-7000/540 ESP, three pressure measurements were taken at the inlet and outlet of the second-stage impeller and the exit of the second diffuser. For the conventional radial pump, pressure measurements were not only made along the flow path but also the inlet and outlet of the pump. As for the facility, a relatively isolated environment was configured due to the glycerin hygroscopic nature, which enabled the precise control of glycerin viscosity.

Before conducting experimental tests, the pump performance in terms of the boosting pressure was verified using water. Due to insufficient power to drive ESP at a higher rotational speed with the extremely viscous working fluid, the performance curves with 720 cP glycerin at 912 rpm are derived from the tests at 800 rpm by applying the similarity law, which is given by

$$Q_2 = Q_1 \frac{N_2}{N_1} \tag{1.15}$$

$$H_2 = H_1 \left(\frac{N_2}{N_1}\right)^2 \tag{1.16}$$

$$BHP_2 = BHP_1 \left(\frac{N_2}{N_1}\right)^3 \tag{1.17}$$

where N is the rotational speed, Q is the flow rate, H is the head, and BHP is the brake horsepower (BHP).

It is revealed that the similarity law works well for *H-Q* performance curves during water test. However, the similarity law does not work for high fluid viscosity tests.

1.6 Monte Verde et al.

Monte Verde et al. (2013) tested P-47, a radial three-stage ESP manufactured by Baker Hughes, at different rotational speeds with the fluid viscosities ranging from 1 to 820 cP. The experimental results were compared with Hydraulic Institute charts. For the correction factors, the real capacity factors based on experimental data varied between 20-45%. As for the hydraulic efficiency, a variance between 25-42% was observed. The most accurate prediction by Hydraulic Institute charts is the pump head with the maximum deviation below 8%. Thus, it was concluded that Hydraulic Institute charts were better to predict pump head rather than efficiency or capacity.

1.7 Sirino et al.

Sirino et al. (2013) studied the viscosity effect on ESP performance using CFD simulation and compared the results with the correspondent experimental measurements by Amaral et al. (2007). A single stage of the GN7000 ESP was used instead of three stages in Amaral et al. (2007) due to the computation cost. Moreover, the balancing holes, casing clearances, and leakage were neglected in the CFD simulation. The schematic of the computational domain is shown in Figure 1.8. For the fluid viscosity over 270 cP, the laminar flow model was employed. For all other simulation cases, the Shear Stress Transport (SST) turbulence model was used even if the real flow case was laminar flow for consistency. The time step used in the CFD simulation is the revolution time for the impeller blade to pass 3.2° displacement.

The water capacity at the BEP is 0.0136 m^3/s at design rotational speed of 3,500 rpm. The water capacity in m^3/s at the low rotational speed is given according to the similarity law:

$$Q_{BEP,w} = \left(\frac{n}{3500}\right) \times 0.0136 \tag{1.18}$$

where n is the rotational speed in rpm.

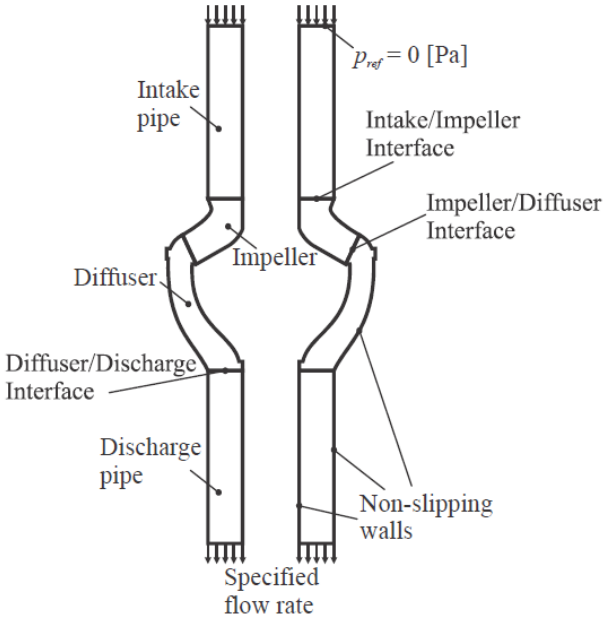

Figure 1.8 Schematic of the Numerical Domain and Boundary Conditions

The numerical results agreed well with the experimental data except for the pressure difference at a low water flow rate and the overestimated efficiency. For low water flow rate, the streamlines in ESP impeller were unstable due to the recirculation flow, which also contributes to the discrepancy of CFD simulation results from correspondent experimental measurements. For the hydraulic efficiency, the ideal assumptions such as neglecting leakage flow cause the over-prediction.

Separations of fluid flow inside an ESP occurred at the inlet of the impeller and the outlet of the diffuser with water at the flow rate of $0.25Q_{BEP,w}$ as illustrated in Figure 1.9, which is the reason the CFD simulated pump head of 60 cP fluid was slightly higher than that of water flow at the low flow rates. However, at higher flow rates, this phenomenon disappeared since the better-oriented streamlines prevailed in the ESP impeller. This helps evaluate the recirculation effect in the mechanistic model developed in this study.

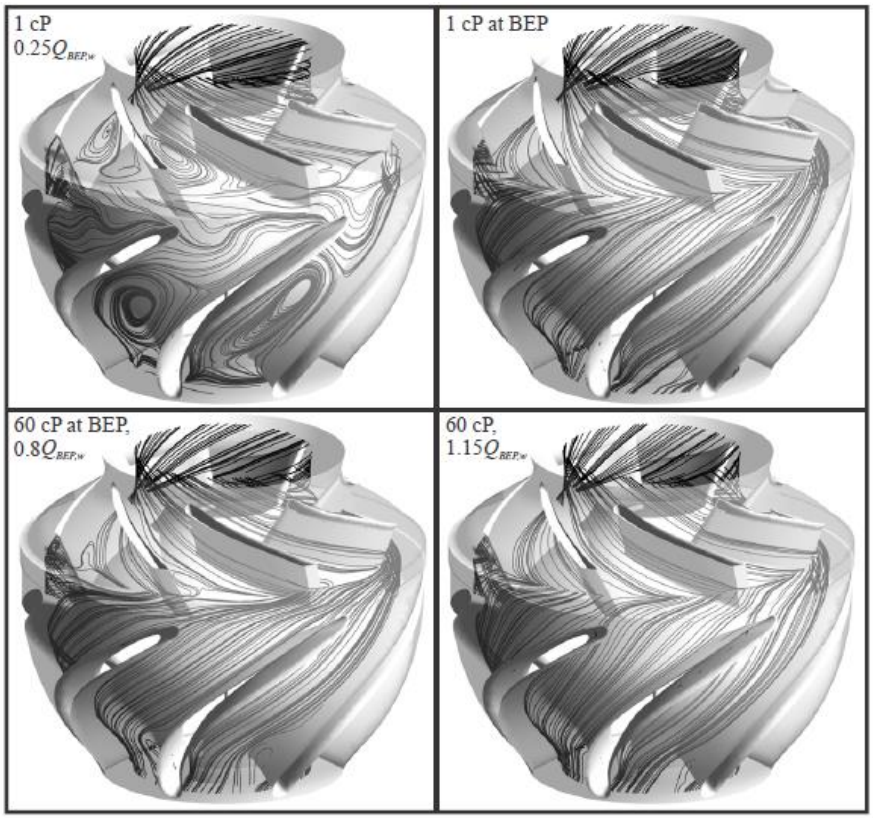

Figure 1.9 Flow Streamlines at a Mid-Surface within Hub and Shroud

Although Sirino et al. proposed new correction factor charts, the field application is limited since the new charts are not based on dimensionless groups but pump dependent.

CHAPTER 2

EXPERIMENTAL FACILITY, PROGRAM AND RESULTS

This chapter presents the experimental results and the detailed information of the test facility and the experimental procedures used to conduct ESP performance tests under viscous fluid flow conditions. The experimental facility comprises a vertical closed liquid flow loop and the data acquisition system (DAQ) is programmed in LabVIEW.

2.1 Test Facility

The schematic of the experimental facility is shown in Figure 2.1. The experimental facility is a modification of a previous gas-liquid flow loop used by Zhu (2017) to measure TE-2700 ESP performances under gassy conditions as shown in Figure 2.2. The old flow loop was connected to an air supply and a 150-barrel horizontal two-phase separator. To test ESP performance under high flow rate and high-viscosity fluid flow conditions, the original air pipeline was disconnected and the liquid flow pipe was extended to install a pipe viscometer. Therefore, the final experimental facility comprises a vertical closed single-phase liquid flow loop as shown in Figure 2.3. The test flow loop can also be viewed in SketchUp with captions shown in Figure 2.4. The flow loop can circulate high viscosity fluids with the flow rate ranges from 0 to 10,000 bpd. The circulated oil viscosity can go up to 1,000 cP and the designed pressure of the flow loop is 300 psia. The detailed specifications and configurations of the equipment used in this flow loop are listed in Appendix A.

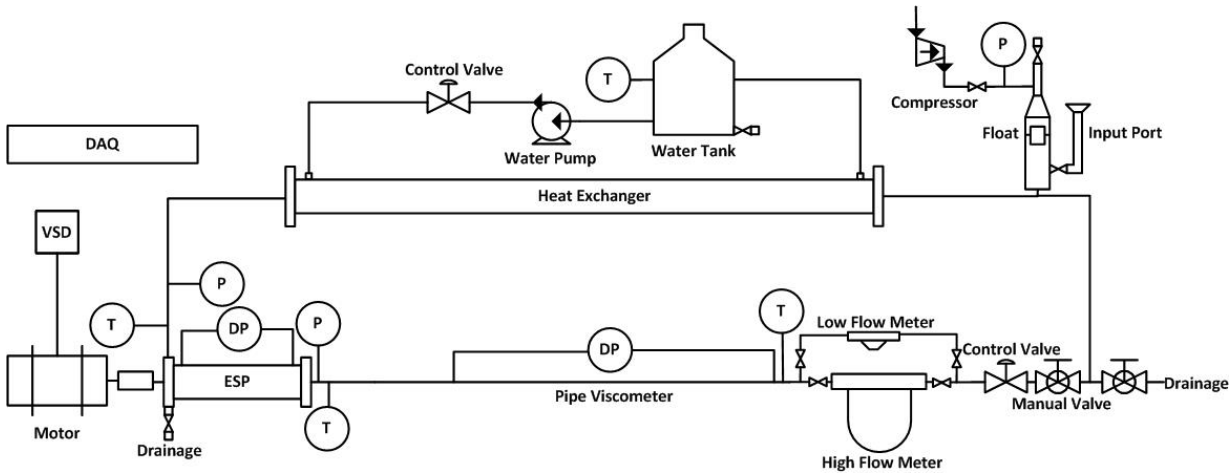

Figure 2.1 Schematic of TUALP High-Viscosity ESP Flow Loop

Figure 2.2 TUALP Gas-Liquid ESP Flow Loop

Figure 2.3 TUALP High-Viscosity ESP Flow Loop

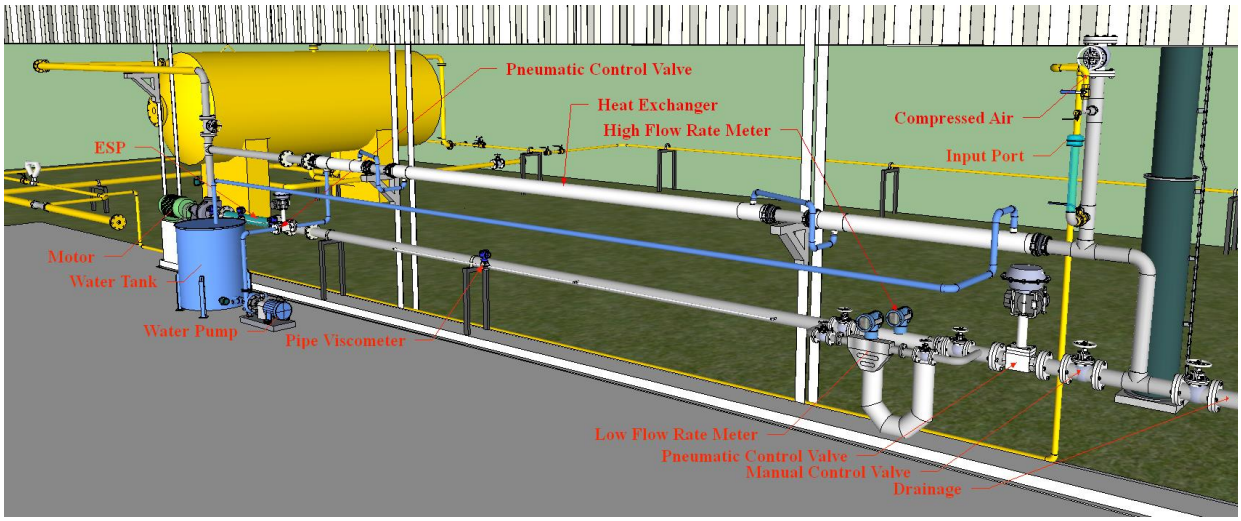

Figure 2.4 TUALP High-Viscosity ESP Flow Loop in SketchUp

2.1.1Test Flow Loop

The test facility is a 3-inch stainless steel flow loop. A variable speed drive (Hitachi L300P) controls rotational speeds of a motor (North American H3650). The motor drives the ESP to pump

the liquid. A torque sensor with a rotational speed sensor (Lebow 1805) is installed on the shaft between the motor and the ESP. To measure ESP performance, there are 7 differential pressure transmitters (Rosemount 3051S), 12 absolute pressure transmitters (Rosemount 2051), 1 resistance temperature detector (RTD), and 1 type J thermocouple. A pipe viscometer consists of a hydraulic development section and a fully developed section covered by a differential pressure transmitter (Rosemount 3051S). The liquid flow velocity profile can fully develop after the 15-foot long hydraulic development section. Then, the differential pressure transmitter measures the pressure drop over the 10- or 20-foot long fully developed section. The pressure drop is a function of the fluid viscosity, the fluid density, the flow rate, the pipe diameter, and the pipe length. The flow rate is measured by a Coriolis flow meter (Micro Motion CMF200) for low flow rates and another Coriolis flow meter (Proline Promass 80E) for high flow rates. A type J thermocouple measures the fluid temperature after flowing through the pipe viscometer. Two globe valves are installed to regulate the flow rates: one is the pneumatic valve and the other one is the manual valve.

Using a clear PVC pipe as the input port, the liquid is filled into the closed loop and the air can be vented. Also, the PVC pipe is a liquid level indicator since it is connected to the main flow loop. A compressor (Kaeser CSD60) pressurizes the flow loop and an air pressure regulator (Speedaire 4ZM22) regulates the flow loop pressure. It keeps the ESP intake pressure higher than the vapor pressure of the fluid to avoid cavitation. Inside the 3-inch venting pipe located at the top of the flow loop, a float is placed to prevent gas entrainment into the liquid during the testing. The float is a hollow stainless steel cylinder with an outer diameter of 2.75 inches and a height of 7.75 inches, as shown in Figure 2.5.

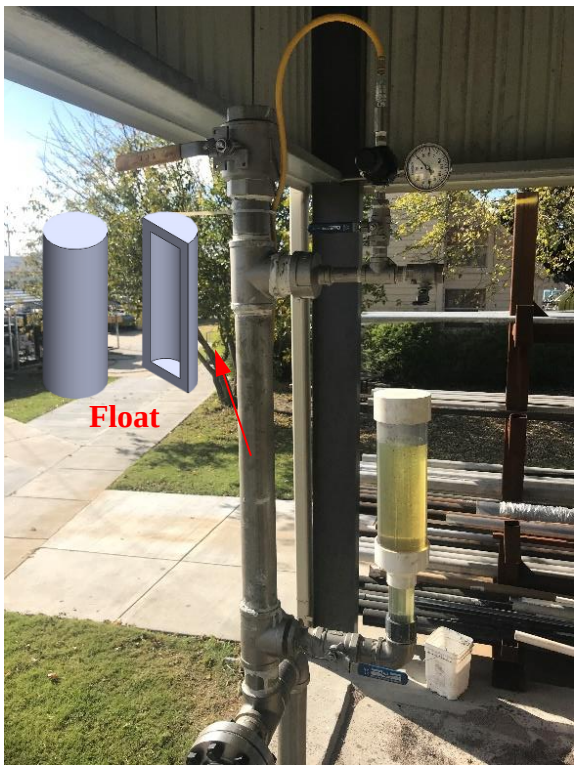

Figure 2.5 Gas Venting Section with a Float inside

The fluid temperature in the flow loop is maintained by a 35-foot long pipe-in-pipe heat exchanger. The outside pipe is the schedule 40 PVC pipe with a nominal diameter of 6 inches. Hot or cold water is stored in a water tank. Another type J thermocouple monitors the water temperature. A water pump (Dayton Stainless Steel Centrifugal Pump 2ZWT9A) circulates the hot or cold water. A 2-inch pneumatic globe valve regulates the flow rate. The operating temperature ranges from 50 to 150 °F corresponding to different working fluid viscosities in the ESP.

2.1.2 Testing ESP

The ESP tested in this study is a 14-stage TE-2700 ESP manufactured by General Electric (GE). The flow rate at the BEP is 2,700 bpd at the rotational speed of 3,500 rpm. At 3,500 rpm, the manufacturer recommended operating range is from 1,500 to 3,300 bpd. The ESP water performance curves vary with rotational speed as shown in Figure 2.6 for head curves, Figure 2.7

for BHP curves, and Figure 2.8 for efficiency curves. With the rotational speed decrease, the head and the BHP decease accordingly. The efficiency curves shift left when the rotational speed decreases. At a constant rotational speed, the head decreases with the increase of liquid flow rates.

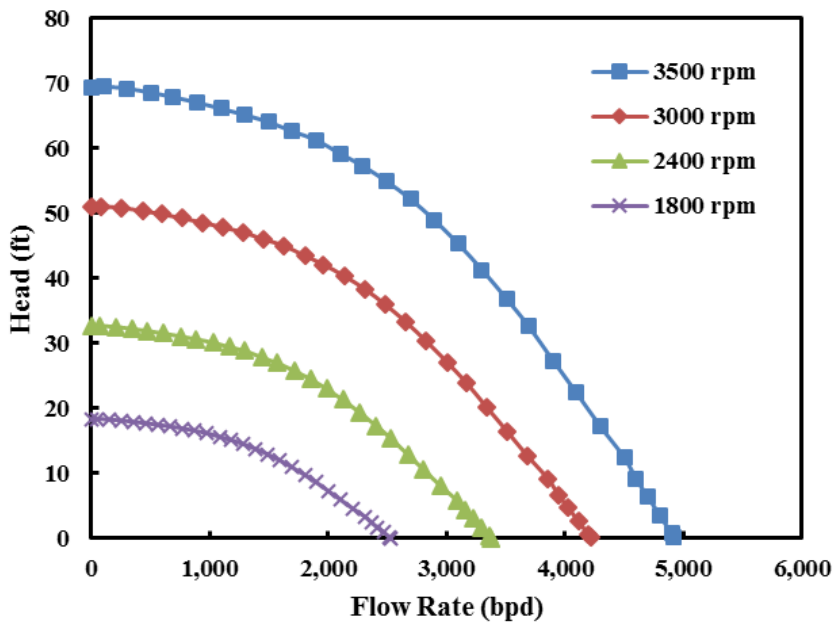

Figure 2.6 TE-2700 ESP Water Performance Curves

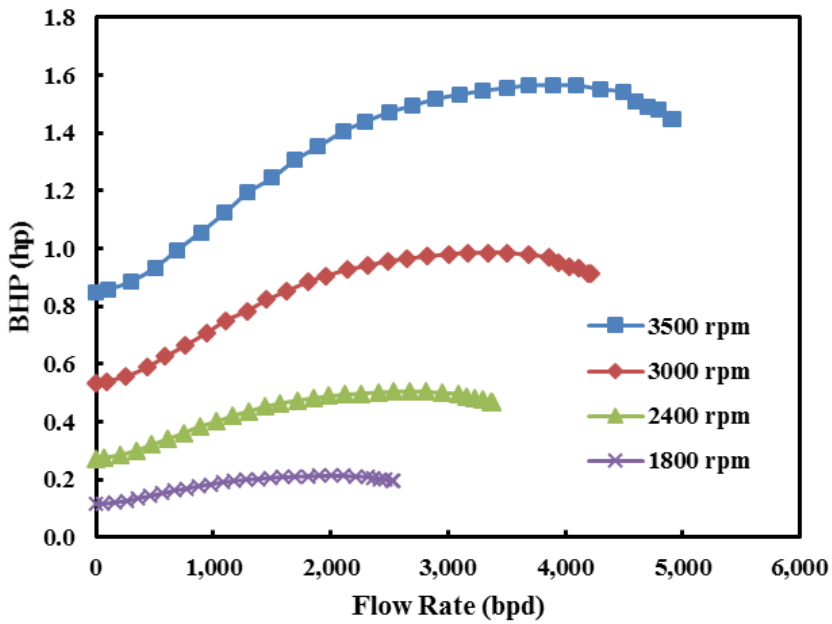

Figure 2.7 TE-2700 ESP BHP Curves

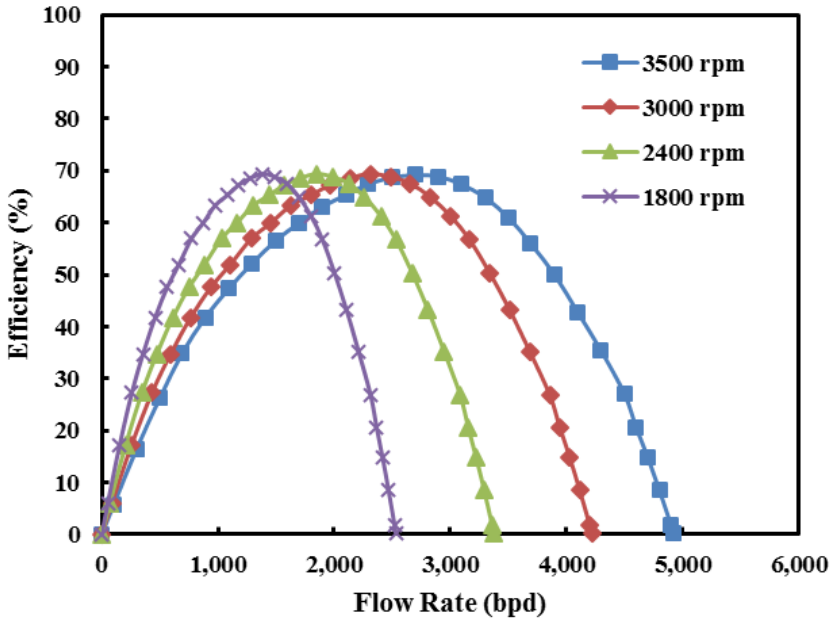

Figure 2.8 TE-2700 ESP Efficiency Curves

2.1.3 ESP Measurements

This TE-2700 ESP has pressure ports drilled at each stage from stage 2 to 14. On the same stage, two ports are perpendicular. Each port is plugged with a quick connector for the pressure measurement. Most pressure transmitters are connected with flexible tubes so that the measured stages can be changed conveniently. In this study, the differential pressures are measured over ESP stages 0-2, 2-3, 3-4, 4-5, 5-6, 6-7, and 4-14. The absolute pressures are measured at ESP intake, stages 2, 3, 4, 5, 6, 7, 8, 9, 10, 11, 12, and 13 to double check the differential pressure measurements. The temperatures are measured at intake of ESP and stage 14.

A torque sensor is used to measure the shaft torque and a passive speed sensor measures the rotational speed. The BHP in hp can be calculated by

$$BHP = \frac{TN}{63025} \tag{2.1}$$

where T is the shaft torque in $lb_f \cdot in$ and N is the shaft rotational speed in rpm.

2.1.4 Data Acquisition System

The instruments are connected with National Instrument (NI) modules so that the instrument input or output signals are packed and transportable. The output signals of pressure transmitters, temperature transmitters, and Coriolis flow meters are transmitted to current input modules (NI cFP-AI-111). The RTD and thermocouples are wired to temperature transmitters (INOR IPAQ R520) to convert signals into 4-20 mA currents. The torque sensor and the passive speed sensor are wired to a torque monitor which transmits voltage signals to a voltage and current input module (NI cFP-AI-110). The control signals for the variable speed drive and pneumatic control valves are wired to a current output module (NI cFP-AO-200). The detailed channel distributions are listed in Appendix B. All modules are mounted on an Ethernet network interface

(NI cFP-1804), which communicates signals to a computer via an Ethernet cable. Using the software NI Measurement & Automation Explorer (MAX), the input signals are collected and the output signals are controlled through the data process computer. Each analog signal is configured and scaled up to the engineering unit in NI MAX, which is written to the *.iak file that can be input to NI LabVIEW for data acquisition and processing.

The DAQ was programmed using the graphical programing language NI LabVIEW V2014. The front panel is shown in Figure 2.9. The DAQ not only serves as a monitor but also works like a controller. With the help of *.iak configuration file, the DAQ can surveil and control the facility. Proportional-integrative derivative (PID) controllers are employed to automatically control the rotational speed, flow rate, and fluid temperature. Figure 2.10 and Figure 2.11 show PID block diagrams in LabVIEW for controlling the flow rate and the fluid temperature, respectively. For convenient control of the facility, a toggle is incorporated to switch between manual and PID controls.

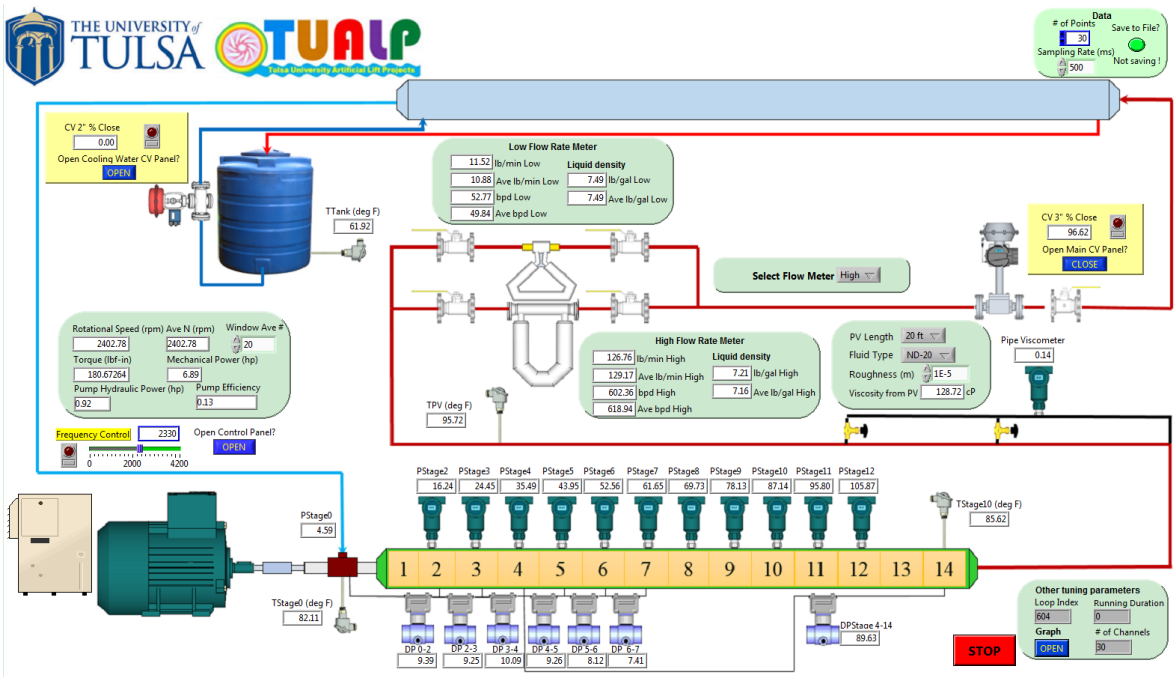

Figure 2.9 DAQ of TUALP High-Viscosity ESP Flow Loop

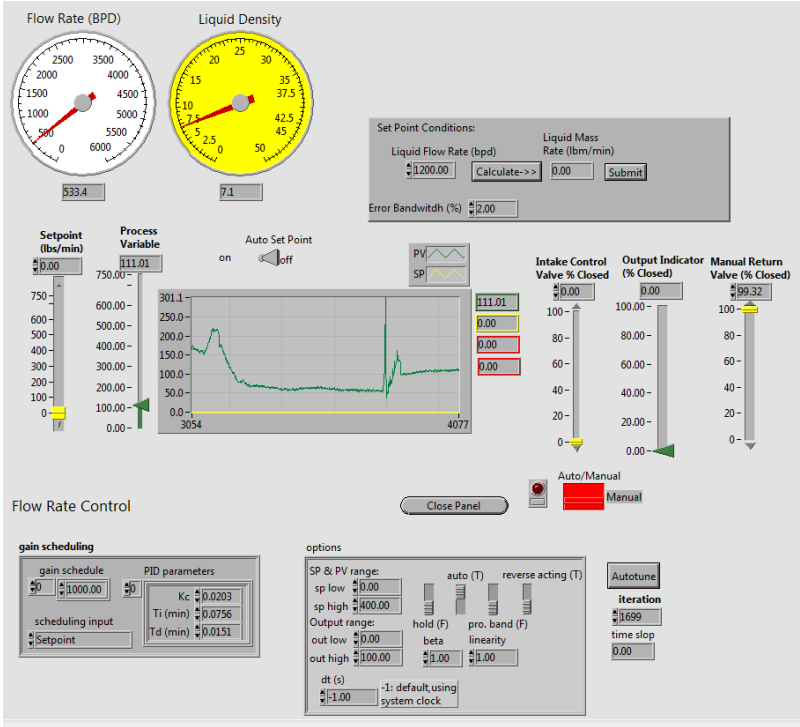

Figure 2.10 Flow Rate PID Control

Figure 2.11 Fluid Temperature PID Control

2.2 Experimental Program

2.2.1 Working Fluids

Tap water and Non-Detergent 20 mineral oil (ND20) are used as the working fluids in this study. Figure 2.12 shows the viscosity changes of ND20 versus temperature. Before testing the viscous oil, the flow loop is filled with tap water so that the ESP performance with water flow is tested. Then, the experimental performance curves are compared with correspondent catalog curves to validate the experimental setup in this study.

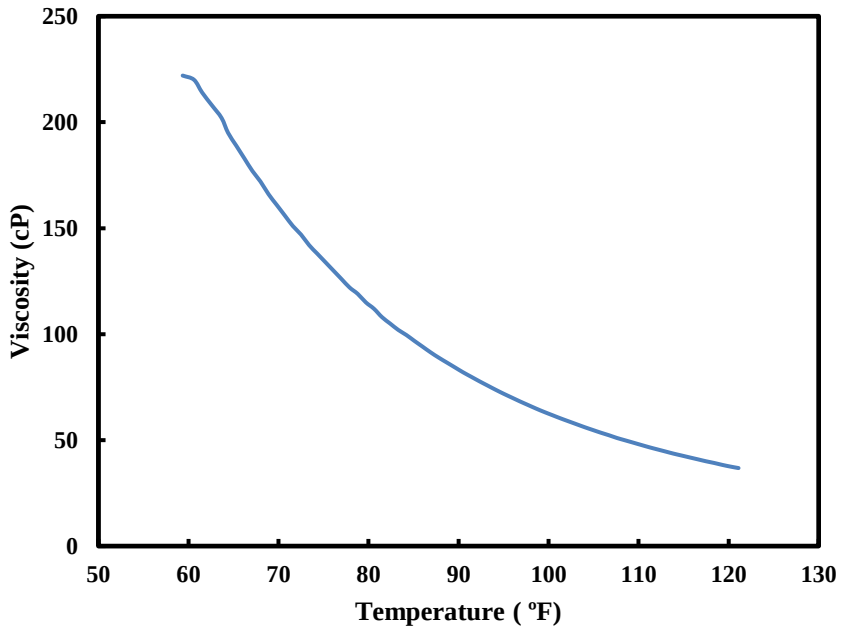

Figure 2.12 ND20 Viscosity versus Temperature

2.2.2 Experimental Procedure

Before testing, the flow loop is filled with the working fluid via the PVC pipe, which also serves as the observation window of the liquid level in the flow loop. When the liquid level reaches the middle of the PVC pipe, the valves near the input port and the compressor are closed. Then,

the ESP is run at different rotational speeds to separate the trapped air in the vertical stainless steel section shown in Figure 2.5. The valve on the upper part of the ventilation pipe is slightly opened to vent the air. Once the air ventilation is completed, the valve near the input port is opened and meanwhile the liquid level in the PVC pipe may drop down. Repeat the previous steps to fill more liquid until the liquid level in the PVC pipe no longer changes.

The flow loop is pressurized to a required value by controlling the air pressure regulator to ensure that the ESP intake pressure is sufficient to avoid cavitation. To obtain the performance curve under a specific flow condition, the ESP is tested at a constant rotational speed with a constant temperature. The rotation speed is adjusted by the variable speed drive. The flow rate is regulated by changing the pneumatic and manual globe valves. The ESP torque, rotational speed, and pressure increment at different flow rates are recorded. The flow rate and the pressure drop over the pipe viscometer are also measured. All the measurements are sampled every half second. For a specific flow condition, 30 samples are stored and the average value is calculated to minimize the uncertainties.

2.2.3 Test Matrix

The test matrix is listed in Table 2.1.

Table 2.1 Experimental Matrix

	Pump Rotational Speed (rpm)	
	2,400	**3,500**
Viscosity (cP)	41, 54, 79, 97, 107	45, 54, 67, 74, 82
Liquid Flow Rate (bpd)	300, 600, 900…	

2.3 Experimental Results

TE-2700 ESP is tested under water flow condition to validate the 3-inch flow loop setup. Then similar experimental tests are conducted under viscous flow conditions.

The head is calculated by

$$H = \frac{\Delta P}{\rho g} \tag{2.2}$$

where ΔP is the differential pressure measured by the differential pressure transmitter and ρ is the liquid density measured by the Coriolis high flow rate meter. Based on the error propagation theory, the error of head is calculated by

$$\Delta H = \sqrt{\left(\frac{\partial H}{\partial(\Delta P)}\Delta(\Delta P)\right)^2 + \left(\frac{\partial H}{\partial \rho}\Delta\rho\right)^2} \tag{2.3}$$

where

$$\frac{\partial H}{\partial(\Delta P)} = \frac{1}{\rho g} \tag{2.4}$$

$$\frac{\partial H}{\partial \rho} = -\frac{DP}{\rho^2 g} \tag{2.5}$$

By substituting correspondent instrument measurement errors listed in Table A.2 into Eq. (2.3), the error of calculated head is within ±1 ft.

The fluid viscosity is calculated by Eq. (C.12) when it is laminar flow. The error of head is calculated by

$$\Delta\mu = \sqrt{\left(\frac{\partial \mu}{\partial(\Delta P)}\Delta(\Delta P)\right)^2 + \left(\frac{\partial \mu}{\partial Q}\Delta Q\right)^2} \tag{2.6}$$

where

$$\frac{\partial \mu}{\partial (\Delta P)} = \frac{556315}{Q} \tag{2.7}$$

$$\frac{\partial \mu}{\partial Q} = -556315 \frac{\Delta P}{Q^2} \tag{2.8}$$

By substituting correspondent instrument measurement errors listed in Table A.2 into Eq. (2.6), the error of calculated fluid viscosity is within ±3 cP.

The hydraulic efficiency is calculated by

$$\eta = \frac{\Delta P Q}{1714 BHP} \tag{2.9}$$

where ΔP is the pressure increment in psi, Q is the volumetric flow rate in gpm, and BHP is the brake horsepower in hp.

2.3.1 Water Performance Curves

TE-2700 ESP is tested with tap water at three different rotational speeds of 2,400 rpm, 3,000 rpm, and 3,500 rpm. Figure 2.13 shows the ESP head curves, Figure 2.14 presents BHP curves, and Figure 2.15 shows hydraulic efficiency curves. The experimental ESP head agrees well with the catalog curves. The measured BHP matches the average BHP from the catalog curves. The BHP is computed based on the rotational speed and the torque. Nevertheless, the detected torque is less than 10% of the measurement range of the torque sensor, resulting in the low resolutions. Thus, only the average BHP value is captured instead of the trend. Due to the reasoning presented above, the hydraulic efficiency curves are lower than the catalog curves at low flow rates but higher at high flow rates.

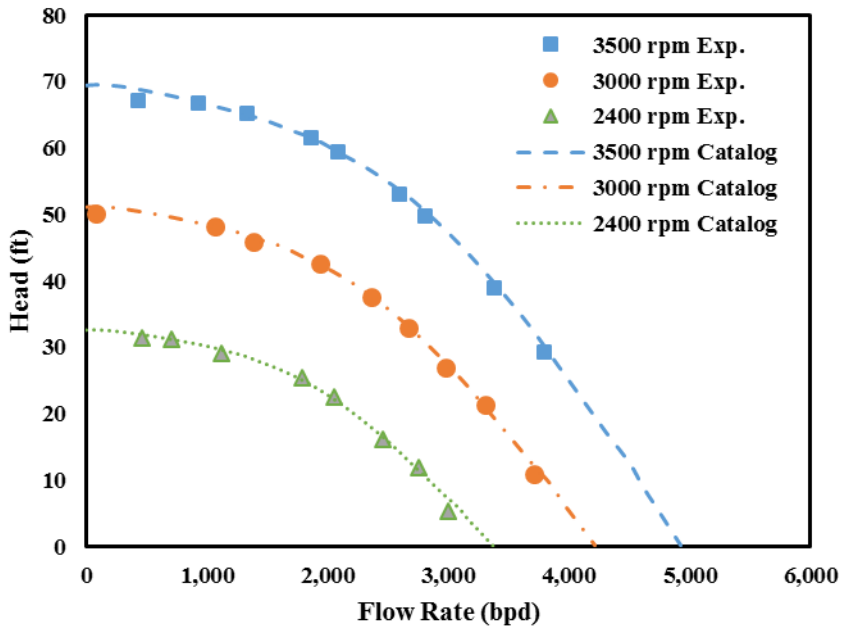

Figure 2.13 TE-2700 ESP Experimental Head with Water

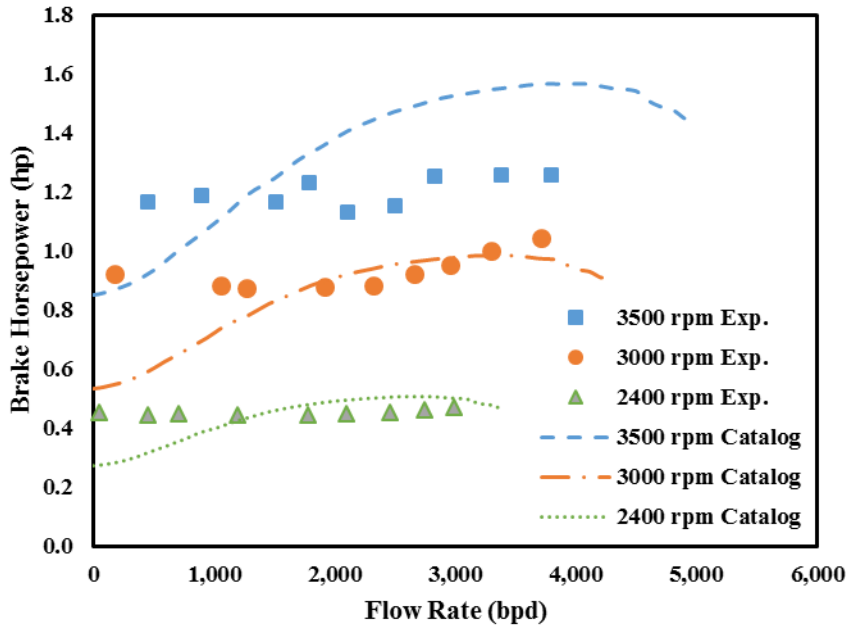

Figure 2.14 TE-2700 ESP Experimental BHP with Water

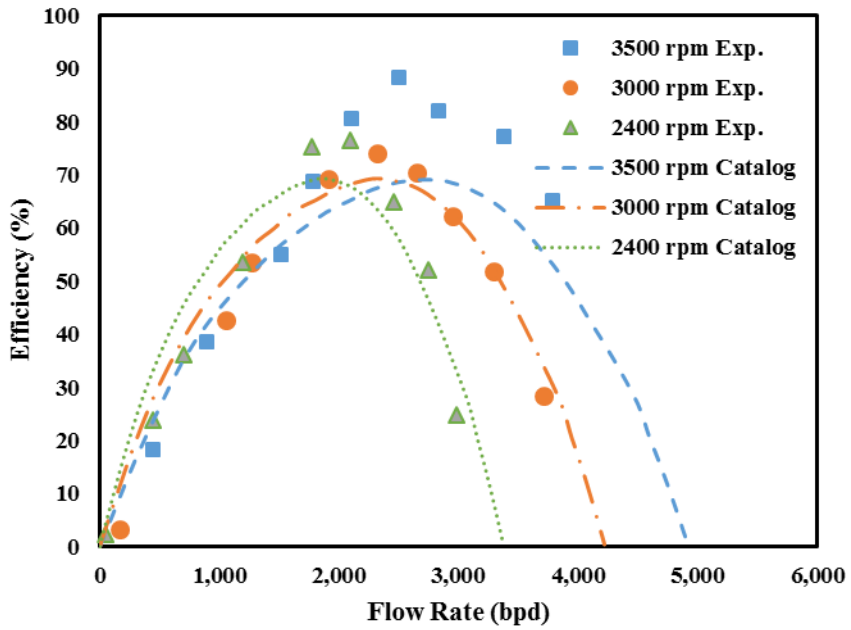

Figure 2.15 TE-2700 ESP Experimental Efficiency with Water

2.3.2 ESP Performance with ND20

The experimental results are presented with two pump rotational speeds at 2,400 rpm and 3,500 rpm. The viscosity of ND20 can be calculated by using the slope of the pressure drop (DP) over the pipe viscometer versus the liquid flow rate. The derivation and viscosity calculation are given in Appendix C.

The TE-2700 ESP head curves with ND20 at 2,400 rpm are shown in Figure 2.16. As can be seen, the pump head deteriorates as the fluid viscosity increases. The ESP head does not change much with varying oil viscosity at low flow rate but larger differences can be observed at the relatively high flow rate.

The TE-2700 ESP head curves with ND20 at the rotational speed of 3,500 rpm are shown in Figure 2.17, where the trends are similar to that at a lower rotational speed of 2,400 rpm.

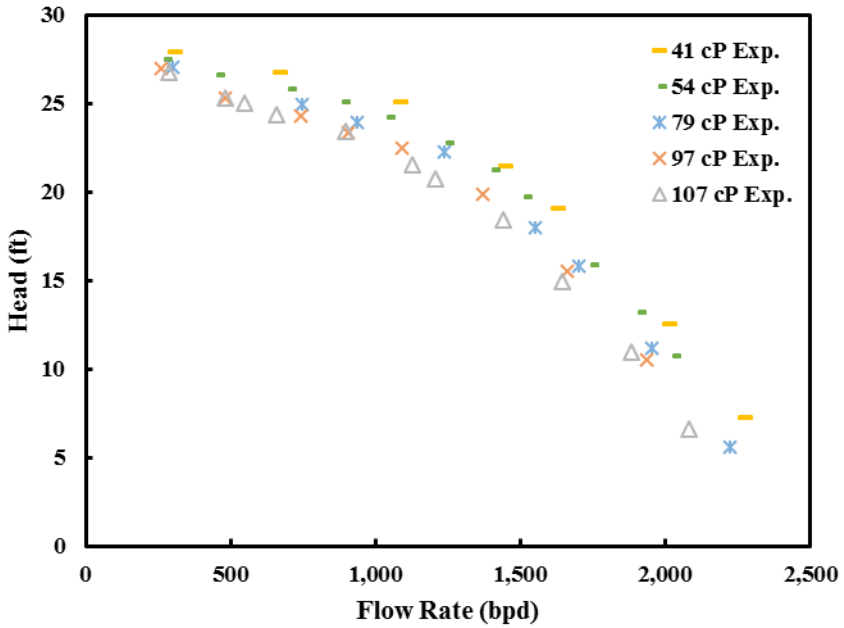

Figure 2.16 TE-2700 ESP Performance with ND20 at 2,400 rpm

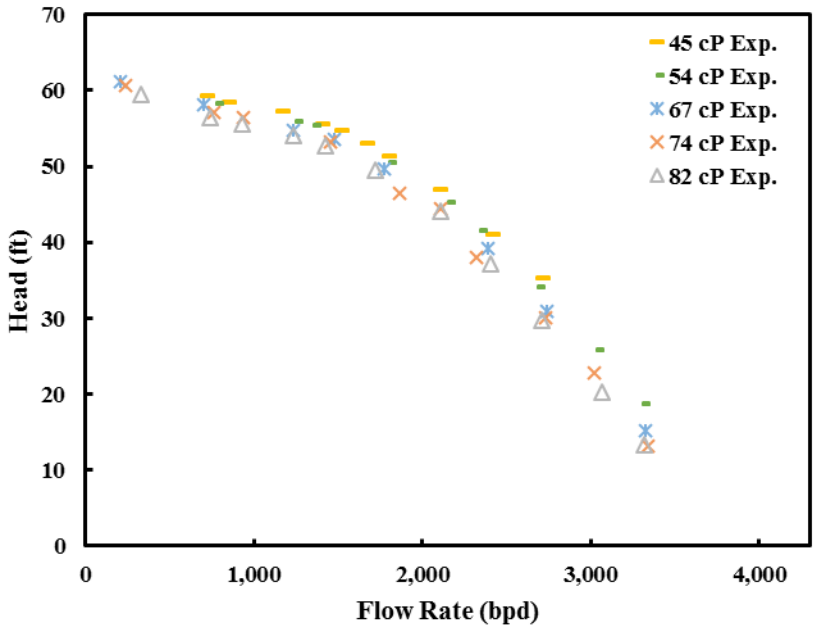

Figure 2.17 TE-2700 ESP Performance with ND20 at 3,500 rpm

CHAPTER 3

THREE-DIMENSIONAL CFD SIMULATION

CFD simulation is a reliable tool to study the flow behaviors and flow structures inside an ESP. Numerical results can further assist the design of the flow loop.

3.1 ESP Geometry and Mesh

The geometry simulated in this study is the TE-2700 ESP. The three-dimensional model of TE-2700 ESP is shown in Figure 3.1 as demonstrated in ANSYS DesignModeler. The impeller is the rotating part and the diffuser is the stationary part during the ESP normal operation.

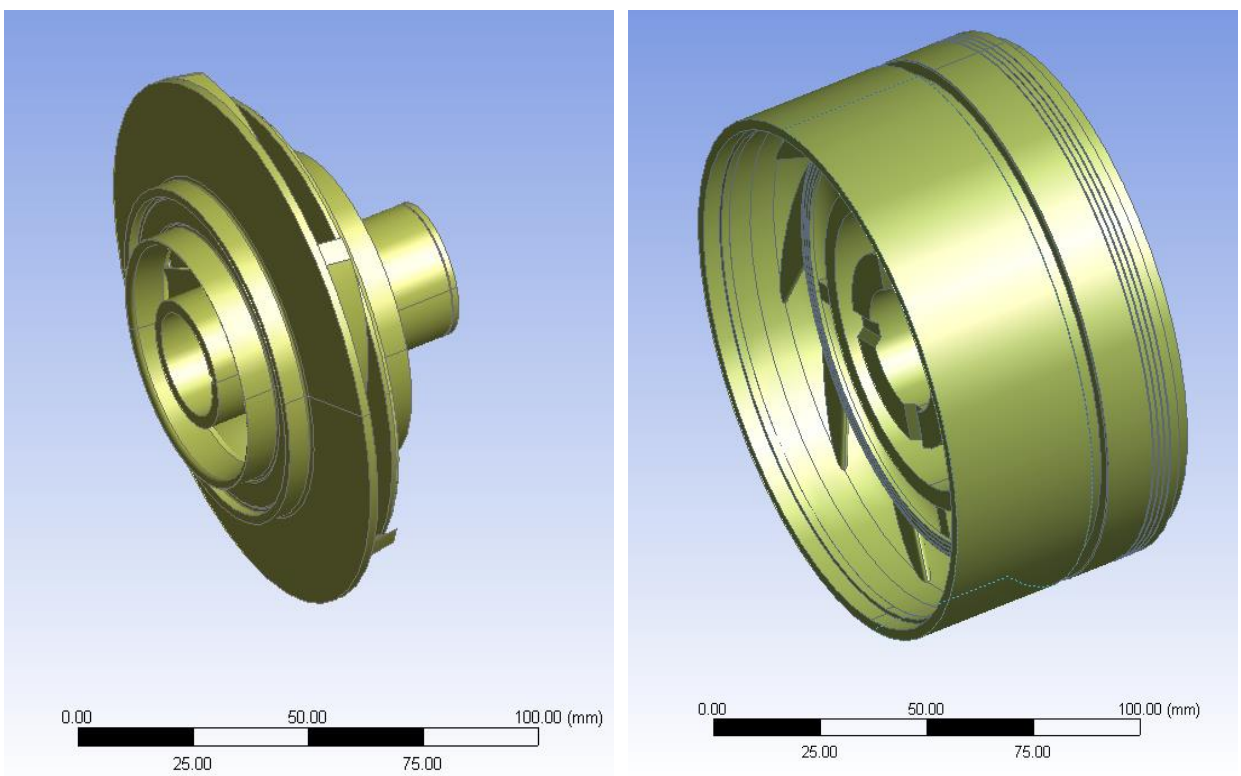

(a) (b)

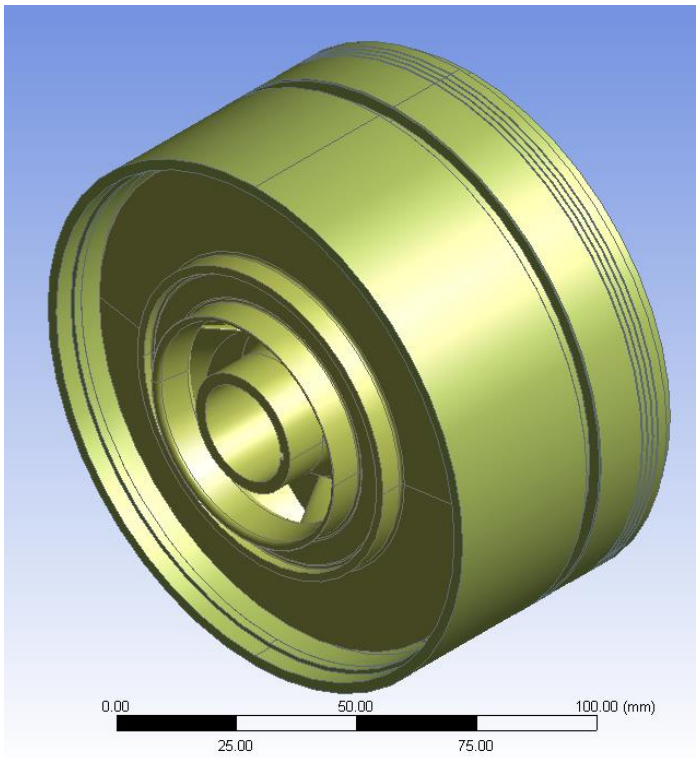

(c)

Figure 3.1 Geometry of TE-2700 ESP (a) Impeller, (b) Diffuser, and (c) Assembly

The fluid domains are extracted from the ESP impeller and diffuser geometry separately. To fill a fluid domain, ANSYS DesignModelers requires inlet and outlet surfaces as well as the flow boundaries of ESP impeller or diffuser geometry to form a cavity which is regarded as the fluid domain in CFD simulation. As a common practice in CFD simulation of centrifugal pump, an interface is created between the impeller and the diffuser flow domains so that the fluid can flow through the rotating and stationary parts freely. Also, the interface serves as the fluid outlet of the impeller and the fluid inlet of the diffuser. To generate the fluid domain in the impeller, the balancing holes on the impeller are removed. The fluid domains of TE-2700 ESP are shown in Figure 3.2.

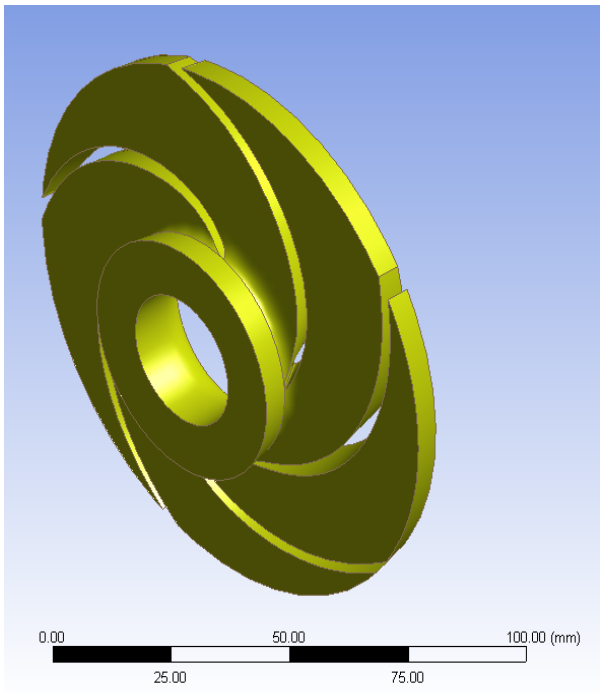

(a)

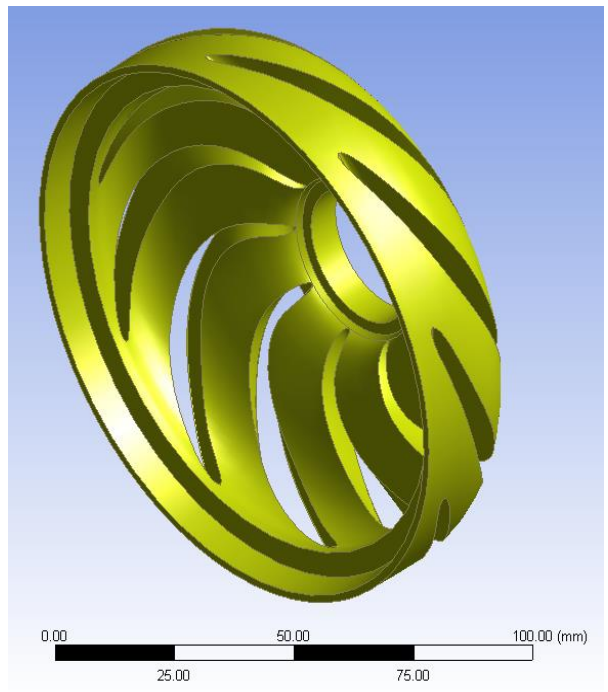

(b)

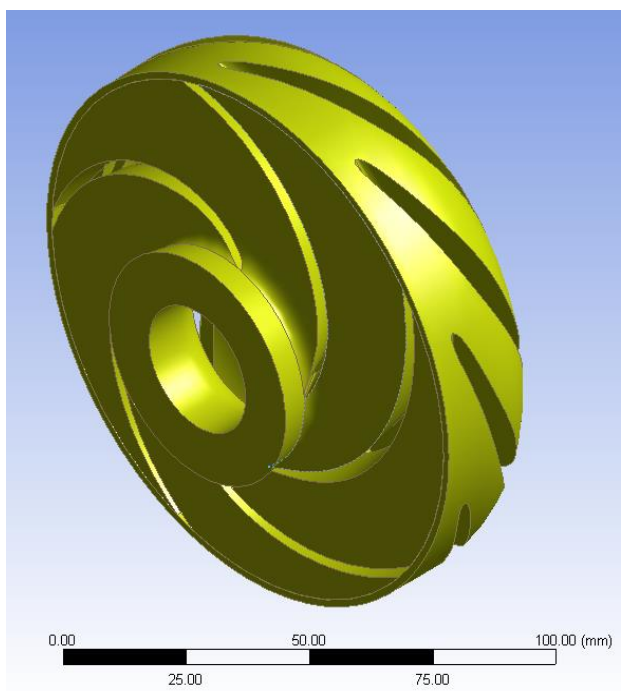

(c)

Figure 3.2 Fluid Domain of TE-2700 ESP (a) Impeller, (b) Diffuser, and (c) Assembly

The unstructured mesh is created in ANSYS ICEM as shown in Figure 3.3. Overall, there are 1,100,548 elements in the impeller fluid domain and 865,922 elements in the diffuser fluid domain. The total mesh grids consist of 1,966,470 elements. The mesh is validated by comparing the simulated ESP head with the catalog curves.

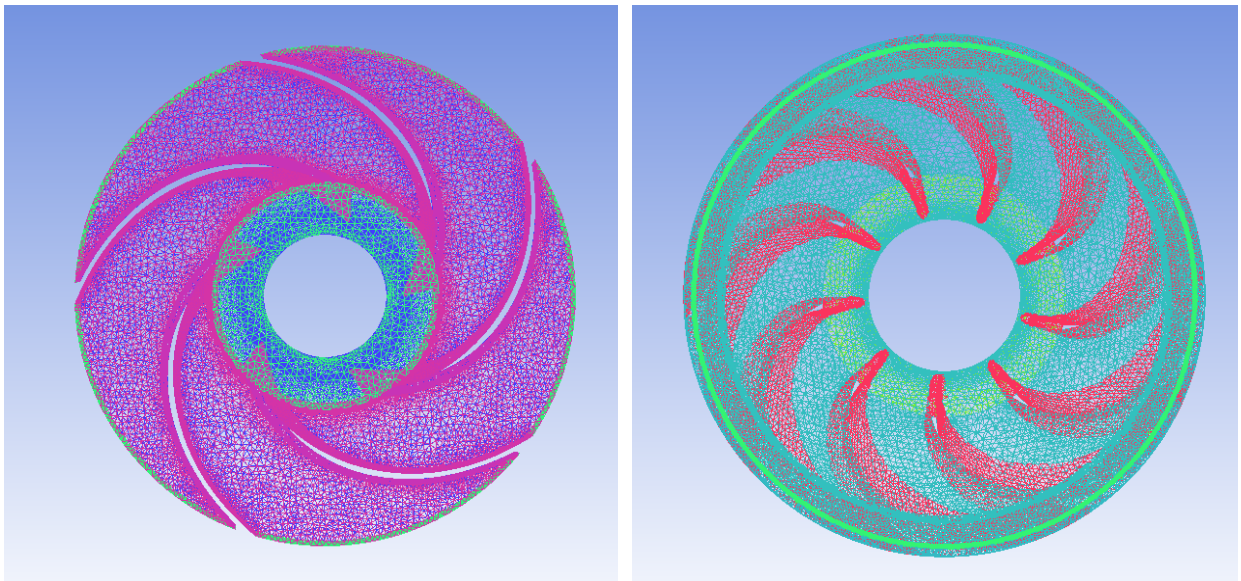

(a) (b)

Figure 3.3 Mesh of TE-2700 ESP (a) Impeller and (b) Diffuser

3.2 CFD Setup

In CFD simulation, only single stage ESP, including a rotating impeller and a stationary diffuser, is used. The shear stress transport (SST) k-ω model is applied in the viscous model in ANSYS Fluent. The testing fluid is liquid water whose properties are provided in ANSYS Fluent database. For CFD simulations with high fluid viscosities, the fluid viscosity changes accordingly while the density remains constant. The impeller fluid domain rotates at 3,500 rpm while the diffuser flow domain is set as stationary. The simulation matrix is shown in Table 3.1. The inlet boundary condition is set as a mass flow inlet while the volumetric flow rate in bpd is used in the

oil production industry. Therefore, the conversion results from the volumetric flow rate in bpd to the mass flow rate in kg/s per a constant water density is shown in Table 3.2. The boundary condition at the diffuser outlet is set as pressure outlet with a fixed value of 170 psia.

Table 3.1 Test Matrix in CFD Simulation

Viscosity (cP)	1, 3, 5, 10, 30, 50, 100, 300, 500, 1,000
Liquid Flow Rate (bpd)	300, 600, 900…

Table 3.2 Flow Rate Conversion

Volumetric Flow Rate (bpd)	**Mass Flow Rate (kg/s)**
300	0.5510
600	1.1021
900	1.6531
1,200	2.2042
1,500	2.7552
1,800	3.3063
2,100	3.8573
2,400	4.4084
2,700	4.9594
3,000	5.5105
3,300	6.0615
3,600	6.6125
3,900	7.1636
4,200	7.7146
4,500	8.2657

3.3 CFD Simulation Results

In each CFD simulation, the head, the hydraulic power, and the BHP are calculated. The head is calculated by

$$H = \frac{P_{outlet} - P_{inlet}}{\rho g} + \frac{{v_{outlet}}^2 - {v_{inlet}}^2}{2g} \tag{3.1}$$

where P_{inlet} and P_{outlet} are static pressures at the impeller inlet and the diffuser outlet, v_{inlet} and v_{outlet} are the average velocities at the impeller inlet and the diffuser outlet, ρ is fluid density, and g is gravitational acceleration.

The meshes with different grid numbers are simulated to check the mesh independence. Figure 3.4 shows that the ESP head becomes constant when the grid number reaches 1,966,470, which proves that the implemented mesh is sufficient.

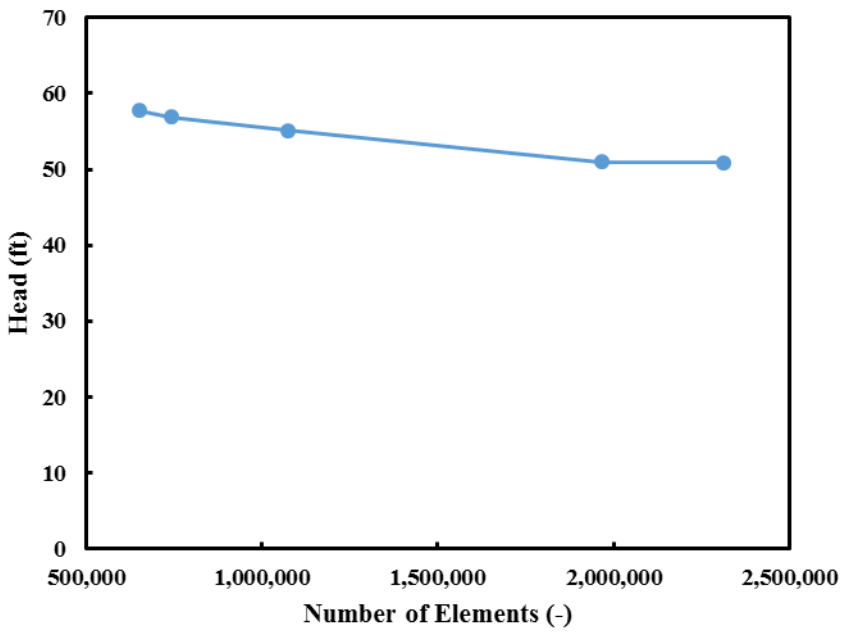

Figure 3.4 TE-2700 ESP CFD Mesh Validation

3.3.1 CFD Simulation with Water

Using water as the working fluid in CFD simulation, the numerical results of ESP head agree well with the catalog curves within the recommended operating range as shown in Figure 3.5. At relatively high flow rates, the simulated boosting pressure is slightly lower.

There is a mismatch between the CFD simulated brake horsepower and the catalog BHP curve. As shown in Figure 3.6, the simulated BHP is lower than the catalog curve at low flow rates,

while it is higher at high flow rates. As a result, the CFD predicted efficiency curve shifts to the left side and the flow rate at the BEP becomes lower as shown in Figure 3.7. Therefore, CFD simulation is better to predict the ESP hydraulic heads rather than BHPs and efficiencies.

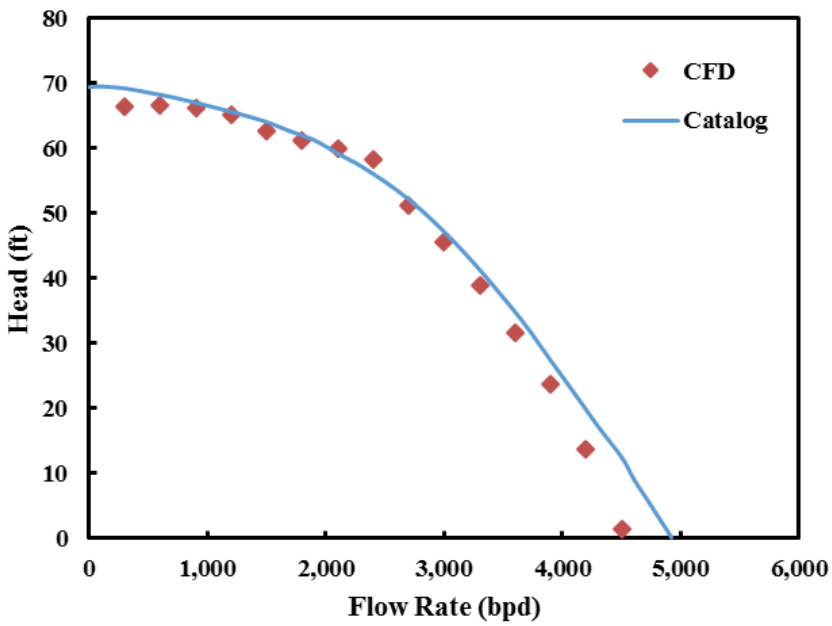

Figure 3.5 CFD Simulation of TE-2700 ESP Water Head

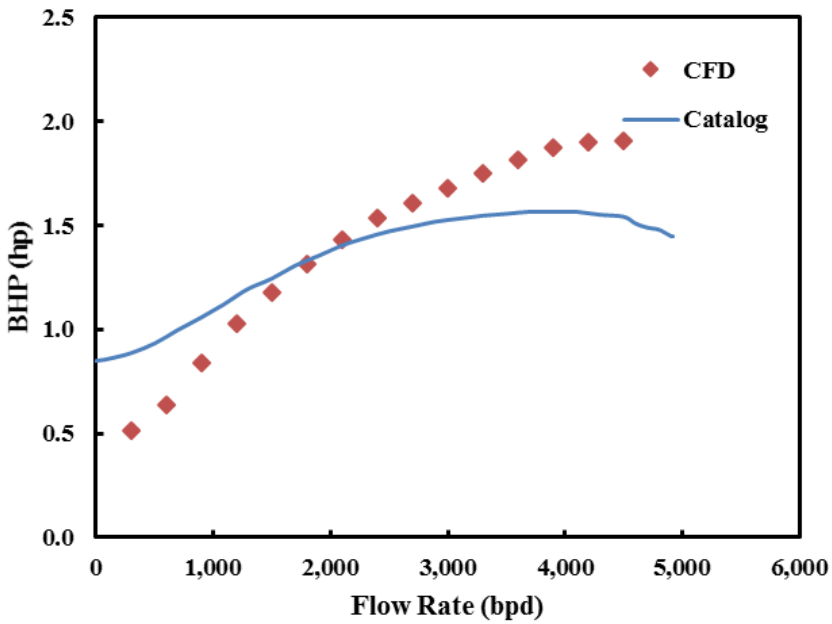

Figure 3.6 CFD Simulation of TE-2700 ESP Water BHP

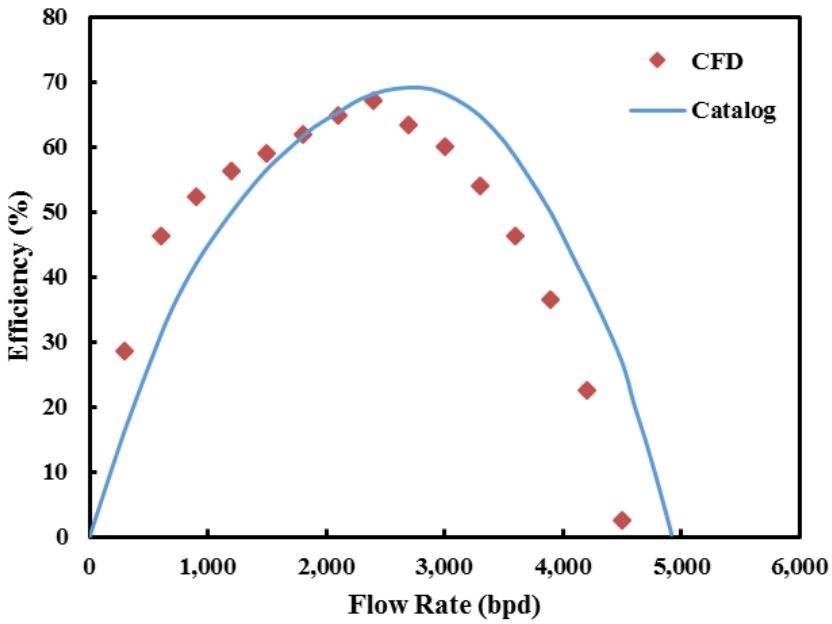

Figure 3.7 CFD Simulation of TE-2700 ESP Water Efficiency

3.3.2 Viscous Fluid Simulation

Figure 3.8 shows the CFD simulation results of ESP head with different fluid viscosities. As the viscosity increases, the pump head decreases. When the fluid viscosity is less than 10 cP, the ESP heads predicted by CFD simulations are very close to the catalog curve. A small variance of ESP head is observed if the liquid flow rate is low since the fluid viscosity mainly affects friction loss and turn loss, which are more dominant at high flow rates. With the oil viscosity of 1,000 cP, the ESP performance curve becomes a linear relationship versus liquid flow rate due to flow regime transition from turbulent flow to laminar flow.

Figure 3.9 shows the CFD simulation results of ESP head compared with experimental data at 3,500 rpm. The experimental data in terms of the head with the oil viscosities of 45, 54, 67, 74, and 82 cP is between the CFD simulation results with the oil viscosities of 100 and 300 cP. Therefore, the CFD simulation underestimates the viscous effect.

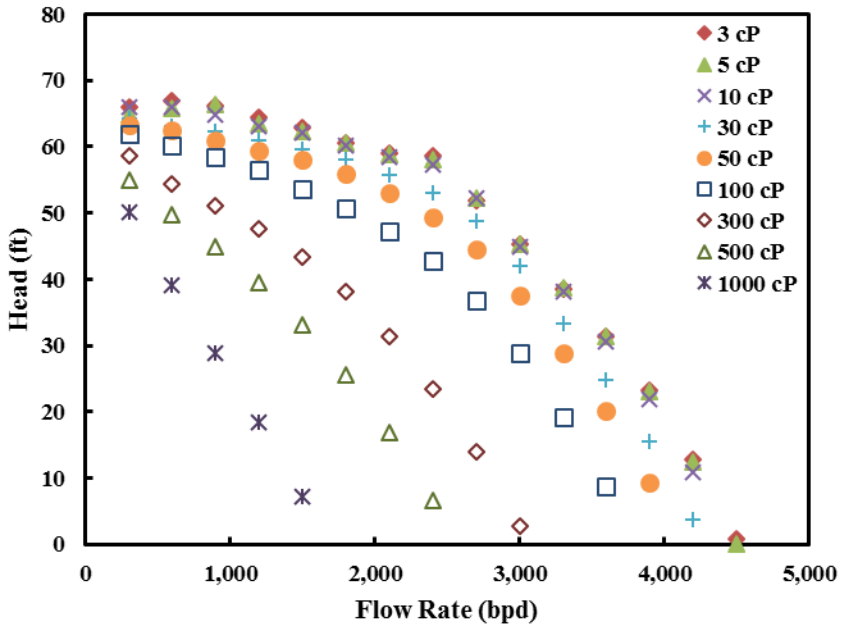

Figure 3.8 CFD Simulation of TE-2700 ESP Head with Viscous Fluid

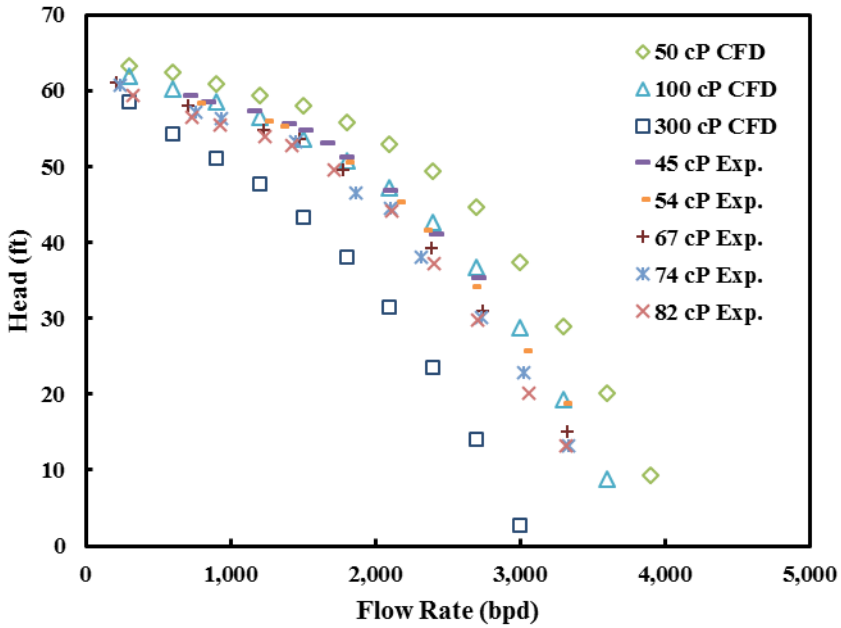

Figure 3.9 TE-2700 ESP Head Comparison of CFD Simulation and Experimental Data

3.3.3 Analysis of Flow

The CFD streamlines with water at different flow rates are shown in Figure 3.10. The water recirculation flow is observed at off-design flow rates. The recirculation is considered as a hydraulic loss especially at low flow rates.

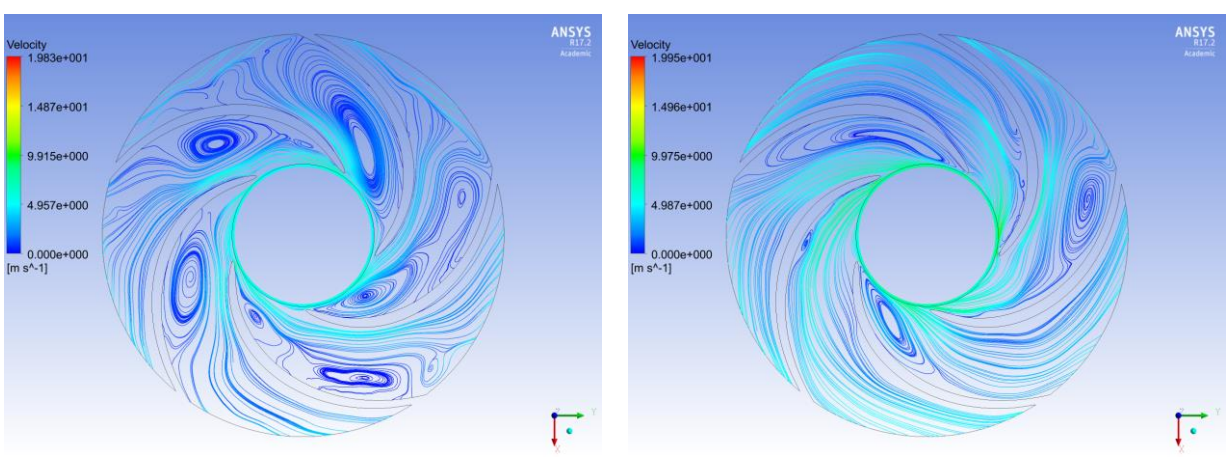

(a) (b)

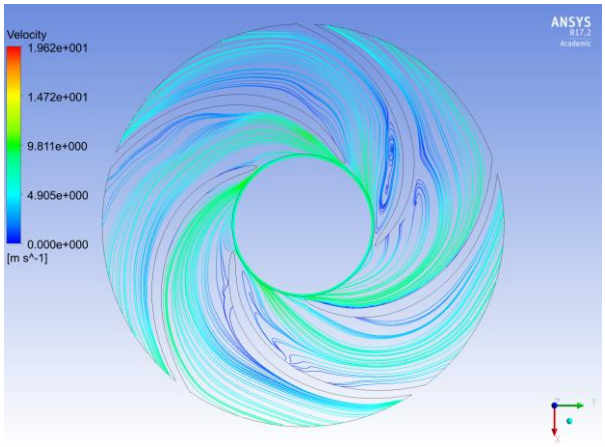

(c)

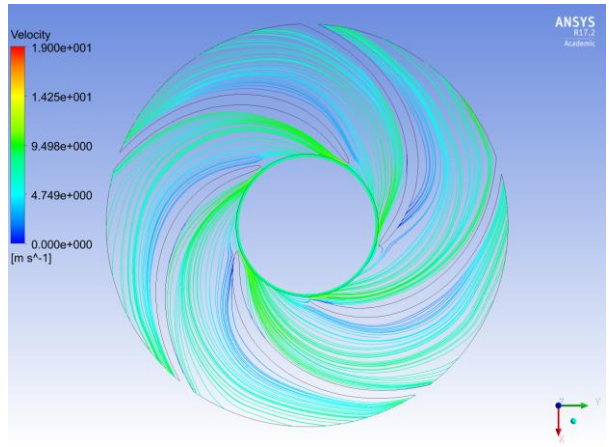

(d)

Figure 3.10 TE-2700 ESP Streamline Comparison with Water at Half Span of Impeller at the Flow Rate of (a) $0.25Q_{BEP}$, (b) $0.50Q_{BEP}$, (c) $0.75Q_{BEP}$, and (d) $1.00Q_{BEP}$

The CFD streamlines with the oil viscosity of 100 cP at different flow rates are similar with the water streamlines as shown in Figure 3.11. However, the recirculation becomes smaller because of the flow regime transition from turbulent to laminar. This observation helps mechanistic modeling of recirculation.

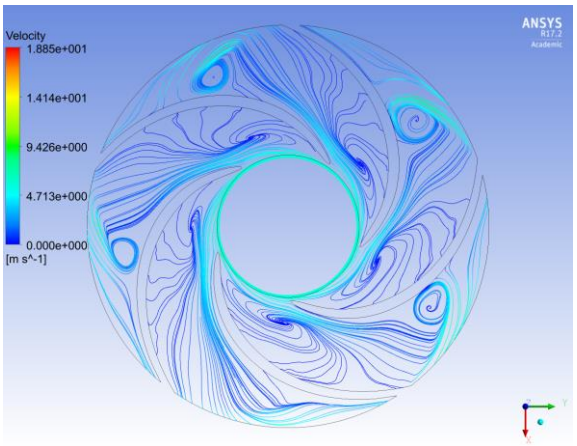

(a)

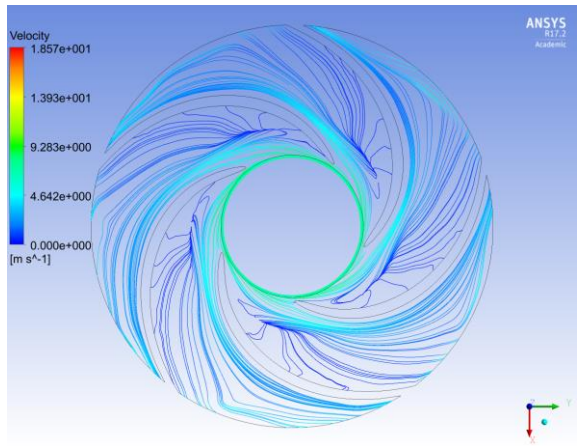

(b)

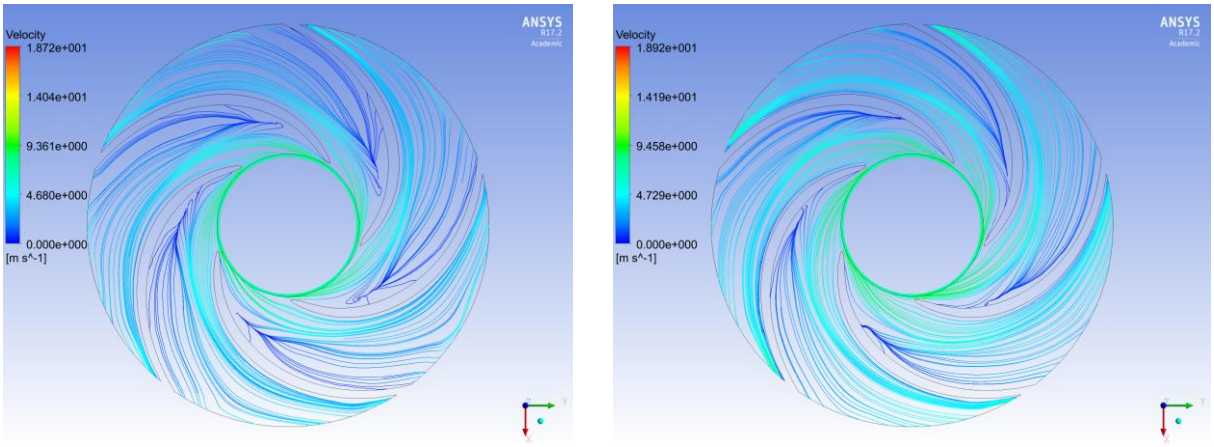

(c) (d)

Figure 3.11 TE-2700 ESP Streamline Comparison at Half Span of Impeller at 100 cP at the Flow Rate of (a) $0.25Q_{BEP}$, (b) $0.50Q_{BEP}$, (c) $0.75Q_{BEP}$, and (d) $1.00Q_{BEP}$

CHAPTER 4

MECHANISTIC MODELING AND RESULTS

This chapter presents a mechanistic model for prediction of ESP hydraulic head under single-phase liquid flow considering fluid viscosity effect. The results are compared with correspondent experimental results.

4.1 Mechanistic Modeling of ESP Single-Phase Liquid Performance

Based on the Euler's equation for the centrifugal pump, the hydraulic losses in an ESP are mechanistically modeled for viscous fluid flow. The model introduces a flow rate at the BMP at which the flow direction at the impeller outlet matches the designed flow direction. If the flow rate is higher or lower than the flow rate at the BMP (Q_{BMP}), the theoretical fluid velocity at the impeller outlet needs to be projected to the flow direction corresponding to the flow rate at the BMP. When the projected velocity is higher than the continuity velocity, the difference is lost due to the recirculation in the impeller. For friction losses in the impeller and diffuser, the friction factors are adjusted considering the flow conditions and geometry of the pump. Losses due to flow direction change and leakage are also included in the model. All equations are in SI units in this chapter.

4.1.1 Euler's Pump Equation inside ESP Impeller

The velocities at impeller inlet and outlet are shown in Figure 4.1. In this figure, R_1 is the radius of the impeller inlet, R_2 is the radius of the impeller outlet, β_1 is the blade angle from

tangential at the impeller inlet, β_2 is the blade angle from tangential at the impeller outlet, U_1 is the impeller tangential velocity at the inlet, U_2 is the impeller tangential velocity at the outlet, W_1 is the fluid relative inlet velocity along the impeller surface, W_2 is the fluid relative outlet velocity along the impeller surface, C_1 is the absolute fluid velocity at the impeller inlet, C_2 is the absolute fluid velocity at the impeller outlet, C_{1M} is the meridional velocity at the impeller inlet, C_{2M} is the meridional velocity at the impeller outlet, C_{1U} is the fluid tangential velocity at the impeller inlet, and C_{2U} is the fluid tangential velocity at the impeller outlet.

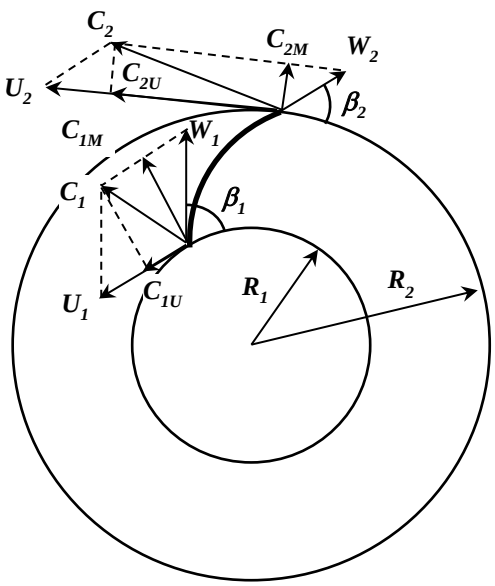

Figure 4.1 Velocity Triangles at Impeller Inlet and Outlet

Euler's pump equation is a basis for centrifugal pump performance prediction shown as

$$H_E = \frac{U_2 C_{2U} - U_1 C_{1U}}{g} \tag{4.1}$$

where H_E is the Euler head and g is the gravitational acceleration. Euler's equation is rewritten based on the velocity trigonometry as

$$H_E = \frac{U_2^2 - U_1^2}{2g} + \frac{W_1^2 - W_2^2}{2g} + \frac{C_2^2 - C_1^2}{2g} \tag{4.2}$$

The three terms on the right-hand side of this equation have physical meanings. The first term is the static head due to the centrifugal forces. The second term is static head due to the velocity change. The third term is the dynamic head.

The impeller angular velocity is

$$\Omega = \frac{2\pi N}{60} \tag{4.3}$$

where N is the rotational speed in rpm. The impeller tangential velocity at the inlet is

$$U_1 = \Omega R_1 \tag{4.4}$$

The impeller tangential velocity at the outlet is

$$U_2 = \Omega R_2 \tag{4.5}$$

The meridional velocity at the impeller inlet is written by

$$C_{1M} = \frac{Q + Q_{LK}}{(2\pi R_1 - Z_I T_B) y_{I1}} \tag{4.6}$$

where Q is the flow rate, Q_{LK} is the leakage flow rate, Z_I is the impeller blade number, T_B is the blade thickness projected to the radial direction, and y_{I1} is the impeller inlet height. The meridional velocity at the impeller outlet is

$$C_{2M} = \frac{Q + Q_{LK}}{(2\pi R_2 - Z_I T_B) y_{I2}} \tag{4.7}$$

where y_{I2} is the impeller outlet height.

The relative velocity with respect to the impeller at the inlet is

$$W_1 = \frac{C_{1M}}{\sin \beta_1} \tag{4.8}$$

The relative velocity with respect to the impeller at the outlet is

$$W_2 = \frac{C_{2M}}{\sin \beta_2} \tag{4.9}$$

The absolute fluid velocity at the impeller inlet is specified as

$$C_1 = \sqrt{C_{1M}^2 + \left(U_1 - \frac{C_{1M}}{\tan\beta_1}\right)^2} \tag{4.10}$$

The absolute fluid velocity at the impeller outlet is specified as

$$C_2 = \sqrt{C_{2M}^2 + \left(U_2 - \frac{C_{2M}}{\tan\beta_2}\right)^2} \tag{4.11}$$

The fluid tangential velocity at the impeller inlet is

$$C_{1U} = U_1 - W_1 \cos\beta_1 \tag{4.12}$$

The fluid tangential velocity at the impeller outlet is

$$C_{2U} = U_2 - W_2 \cos\beta_2 \tag{4.13}$$

Substituting Eq. (4.12) and (4.13) into Eq. (4.2), the Eq. (4.2) is rewritten as

$$H_E = \frac{U_2(U_2 - W_2\cos\beta_2) - U_1(U_1 - W_1\cos\beta_1)}{g} \tag{4.14}$$

If the fluid is not rotating when entering the impeller, $C_{1U} = 0$ and $C_1 = C_{1M}$, velocity triangles change as shown in Figure 4.2. Therefore, Eq. (4.14) can be rewritten as

$$H_E = \frac{U_2^2}{g} - \frac{U_2 C_{2M}}{g\tan\beta_2} \tag{4.15}$$

Wiesner (1967) proposed an equation to consider the finite blade effect so Eq. (4.15) is rewritten as

$$H_E = \sigma_s \frac{U_2^2}{g} - \frac{U_2 C_{2M}}{g\tan\beta_2} \tag{4.16}$$

where σ_s is the slip coefficient, which is calculated by

$$\sigma_s = 1 - \frac{\sqrt{\sin\beta_2}}{Z_I^{0.7}} \tag{4.17}$$

For this mechanistic model, the slip coefficient is redefined as

$$\sigma_s = 1 - \frac{\sqrt{\sin\beta_2}}{Z_I^{1.4\times\left(\frac{3448}{N_s}\right)^{0.4}}} \tag{4.18}$$

where N_s is the specific speed which can be calculated as

$$N_s = \frac{\sqrt{q_{bep}}N}{H_{bep}^{3/4}} \tag{4.19}$$

where q_{bep} is the pump capacity at the BEP in gpm, N is the impeller rotational speed in rpm, and H_{bep} is the pump head at the BEP in ft.

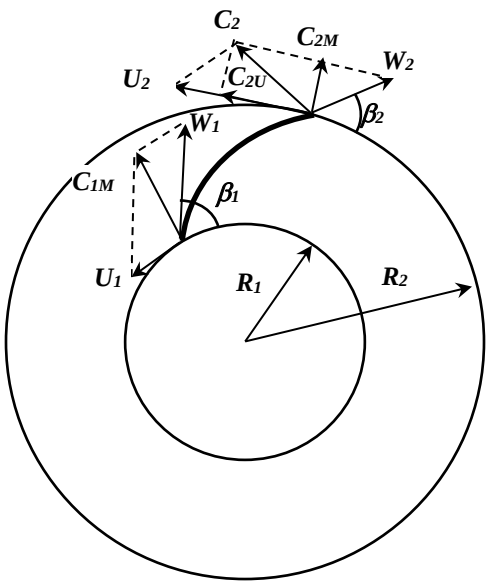

Figure 4.2 Velocity Triangles without Inlet Rotation

4.1.2 Effective Velocity at Impeller Outlet

The direction of the fluid absolute velocity at the impeller outlet is assumed to match the designed flow direction from the impeller to the diffuser at the flow rate at the BMP. An effective velocity is applied when the flow rate is smaller or larger than the flow rate at the BMP.

Figure 4.3 shows the velocities at the impeller outlet when the flow rate is less than the flow rate at the BMP. In this figure, C_{2B} is the absolute fluid velocity at the impeller outlet corresponding to the flow rate at the BMP, C_{2MB} is the meridional velocity at the impeller outlet corresponding to the flow rate at the BMP, W_{2B} is the fluid relative outlet velocity along the impeller surface corresponding to the flow rate at the BMP, C_{2F} is the fluid flow velocity outside the impeller, C_{2P} is the projection of C_2 in the direction of C_{2B}, and V_S is the shear velocity.

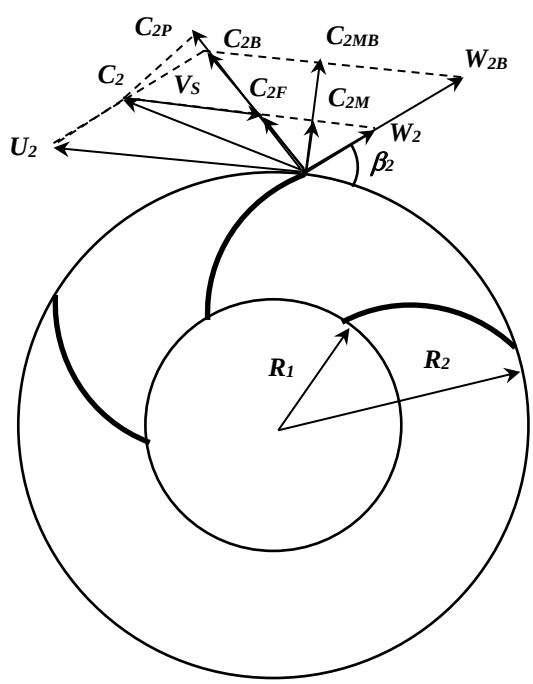

Figure 4.3 Velocity Triangles at Impeller Outlet for $Q + Q_{LK} < Q_{\mathrm{BMP}}$

When the flow rate is smaller than the flow rate at the BMP, the fluid flow velocity outside the impeller is

$$C_{2F} = C_{2B}\frac{Q + Q_{LK}}{Q_{BMP}} \tag{4.20}$$

The shear velocity is

$$V_S = U_2\frac{Q_{BMP} - (Q + Q_{LK})}{Q_{BMP}} \tag{4.21}$$

The projections of C_2 and V_S on the perpendicular direction of C_{2B} are the same, which can be derived as

$$C_2^2 - C_{2P}^2 = V_S^2 - (C_{2P} - C_{2F})^2 \tag{4.22}$$

C_{2P} is solved as

$$C_{2P} = \frac{C_2^2 + C_{2F}^2 - V_S^2}{2C_{2F}} \tag{4.23}$$

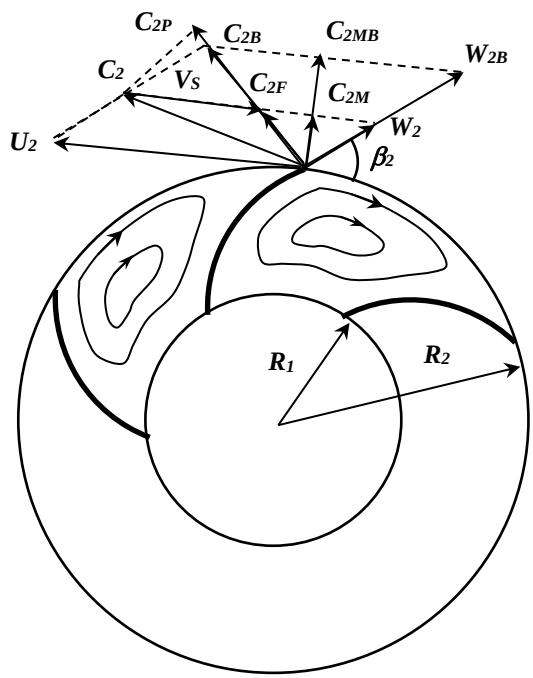

Figure 4.4 Velocity Triangles at Impeller Outlet for $Q + Q_{LK} < Q_{\mathrm{BMP}}$

The shear effect makes the fluid recirculate inside the impeller as shown in Figure 4.4. Consequently, only part of the theoretical kinetic energy is transferred to static pressure. The recirculation depends on the shear velocity, the impeller channel size, and the fluid viscosity. A Reynolds number is obtained to estimate the recirculation effect as

$$Re_C = \frac{\rho V_S D_C}{\mu} \tag{4.24}$$

where D_C is the representative impeller channel width at the outlet in flow direction and it can be found by

$$D_C = \frac{2\pi R_2}{Z_I} \sin \beta_2 - T_B \tag{4.25}$$

To define the effective velocity change, a velocity reduction factor due to the recirculation is described as

$$\sigma = \frac{\left(\frac{\mu_w}{\mu}\right)^{0.1}}{10 + 0.02 Re_C^{0.2}} \tag{4.26}$$

where μ_w is water viscosity. A correlation of effective velocity based on comparisons with experimental results is defined as

$$C_{2E} = C_{2F} + \sigma(C_{2P} - C_{2F}) \tag{4.27}$$

Figure 4.5 shows the velocities at the impeller outlet when the flow rate is higher than the flow rate at the BMP. In this scenario, the shear velocity is calculated by

$$V_S = U_2 \frac{(Q + Q_{LK}) - Q_{BMP}}{Q_{BMP}} \tag{4.28}$$

The rest formulae used are the same when the flow rate is smaller the flow rate at the BMP. The effective velocity becomes:

$$C_{2E} = C_{2F} + \sigma(C_{2P} - C_{2F}) \frac{Q + Q_{LK} - Q_{BMP}}{Q_{BMP}} \tag{4.29}$$

For all the flow rates, the effective Euler head is found as

$$H_{EE} = H_E + \frac{C_{2E}^2 - C_2^2}{2g} \tag{4.30}$$

The flow rate at the BMP is changed with rotational speed and fluid viscosity. A correlation is described as

$$Q_{BMP} = Q_{BMP,ref} \frac{N}{N_{ref}} \left(\frac{\mu}{\mu_w}\right)^{\frac{34.48}{N_S}} \tag{4.31}$$

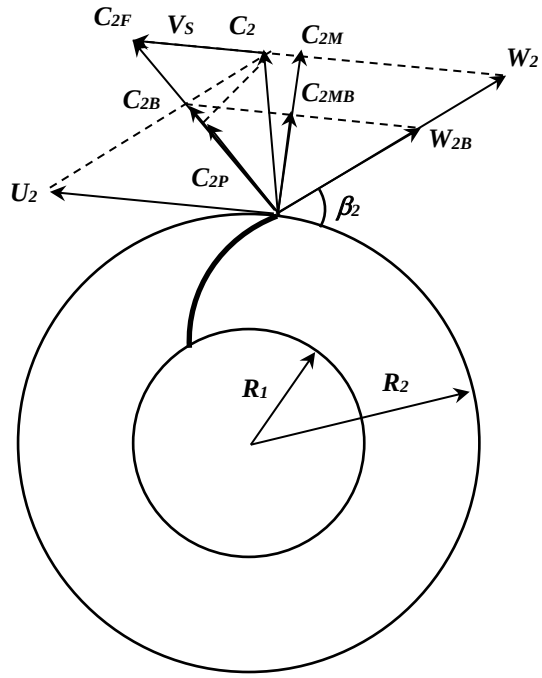

Figure 4.5 Velocity Triangles at Impeller Outlet for $Q + Q_{LK} > Q_{\mathrm{BMP}}$

4.1.3 Head Losses

The frictions losses happen when the fluid flows through the impeller and diffuser. The liquid flows from the impeller to the diffuser and from the diffuser to the inlet of the next stage impeller. The flow direction changes cause head losses. The balancing holes on the impeller hub cause the fluid leakage which reduces the pump head, especially at relatively low flow rates.

To evaluation the friction losses, the fluid flows inside the impeller and diffuser is treated as channel flows. Thus, the friction losses in the impeller can be expressed as

$$H_{FI} = f_{FI}\frac{(W_1 + W_2)^2 L_I}{8gD_I} \tag{4.32}$$

where f_{FI} is the Moody friction factor, L_I is the channel length, and D_I is the representative (hydraulic) diameter of the channel.

The friction loss in the diffuser can be estimated by

$$H_{FD} = f_{FD} \frac{{V_D}^2 L_D}{2gD_D} \tag{4.33}$$

where f_{FD} is the Moody friction factor, V_D is the representative fluid velocity, L_D is the channel length, and D_D is the representative (hydraulic) diameter of the channel.

The Moody friction factor is a function of Reynolds number and relative roughness of the walls. Churchill (1977) equations are used to calculate the Moody friction factor. The representative Reynolds numbers in the impeller and diffuser are

$$Re_I = \frac{\rho V_I D_I}{\mu} \tag{4.34}$$

where V_I is the representative fluid velocity, and

$$Re_D = \frac{\rho V_D D_D}{\mu} \tag{4.35}$$

The representative diameter of the impeller channel is defined as

$$D_I = \frac{4Vol_I}{A_{SI}} \tag{4.36}$$

where Vol_I is the volume of an impeller channel and A_{SI} is the total wall area of an impeller channel. Similarly, the representative diameter of the diffuser channel is given by

$$D_D = \frac{4Vol_D}{A_{SD}} \tag{4.37}$$

where Vol_D is the volume of a diffuser channel and A_{SD} is the total wall area of a diffuser channel.

The representative fluid velocity in the impeller channel is

$$V_I = \frac{Q + Q_{LK}}{A_I Z_I} \tag{4.38}$$

where A_I is the representative impeller channel cross sectional area and Z_I is the impeller blade number. The representative fluid velocity in the diffuser channel is

$$V_D = \frac{Q}{A_D Z_D} \tag{4.39}$$

where A_D is the representative diffuser channel cross sectional area and Z_D is the diffuser vane number.

Here, A_I and A_D are defined as

$$A_I = \frac{Vol_I}{L_I} \tag{4.40}$$

and

$$A_D = \frac{Vol_D}{L_D} \tag{4.41}$$

The head losses due to turns is caused by the changes of flow directions when fluid flows from the impeller outlet to the diffuser inlet and from the diffuser outlet to the impeller inlet of the next stage. The head losses for the turns in impeller and diffuser can be estimated as

$$H_{TI} = f_{TI} \frac{V_I^2}{2g} \tag{4.42}$$

and

$$H_{TD} = f_{TD} \frac{V_D^2}{2g} \tag{4.43}$$

where f_{TI} and f_{TD} are the local drag coefficients, which are determined from experiments. The ratio of f_{TI} to f_{TD} is

$$\frac{f_{TI}}{f_{TD}} = \frac{\frac{R_2 - R_1}{L_I}}{\frac{R_{D1} - R_{D2}}{L_D}} \tag{4.44}$$

where R_{D1} is the radius of the diffuser inlet and R_{D2} is the radius of the impeller outlet.

As for leakage losses, since the fluid rotation is caused by only one side, half of the tangential velocity of the impeller rotation may be counted. The leakage losses can be estimated

as

$$H_{LK} = H_{IO} - \frac{U_2^2 - U_{LK}^2}{8g} \tag{4.45}$$

where H_{IO} is the head increase across the impeller and U_{LK} is the tangential velocity due to the impeller rotation at the leakage. The head increase by the impeller can be estimated as

$$H_{IO} = H_{EE} - H_{FI} - H_{TI} \tag{4.46}$$

The tangential velocity due to the impeller rotation at the leakage is

$$U_{LK} = \Omega R_{LK} \tag{4.47}$$

where R_{LK} is the radius corresponding to the leakage.

The head loss across the leakage consists of contraction, expansion, and friction components, which is calculated by

$$H_{LK} = 0.5\frac{V_L^2}{2g} + 1.0\frac{V_L^2}{2g} + f_{LK}\frac{V_L^2 L_G}{2gS_L} \tag{4.48}$$

where L_G is the leakage channel length and S_L is the width of the leakage.

Therefore, the fluid velocity through the leakage can be calculated by

$$V_L = \sqrt{\frac{2gH_{LK}}{f_{LK}\frac{L_G}{S_L} + 1.5}} \tag{4.49}$$

Assuming smooth leakage channel, the friction factor f_{LK} can be estimated by Churchill (1977) equations when the Reynolds number is defined as

$$Re_L = \frac{\rho V_L S_L}{\mu} \tag{4.50}$$

Then, the leakage flow rate can be calculated by

$$Q_{LK} = 2\pi R_L S_L V_L \tag{4.51}$$

4.2 Mechanistic Modeling Setup

The pump heads predicted by the mechanistic model are compared to the available experimental data. The experimental results comprise of the TE-2700 ESP conducted in this study and the GC-6100 ESP provided by Baker Hughes.

4.2.1 TE-2700 ESP Setup

TE-2700 ESP is a radical flow pump with a specific speed of 1,600. The geometrical parameters of TE-2700 ESP are the inputs of the mechanistic model.

The new model is adjusted to match the catalog water head curve by finding the flow rate at the BMP, which is 3,400 bpd. As shown in Figure 4.6, the water head predicted by this mechanistic model matches the catalog performance curve.

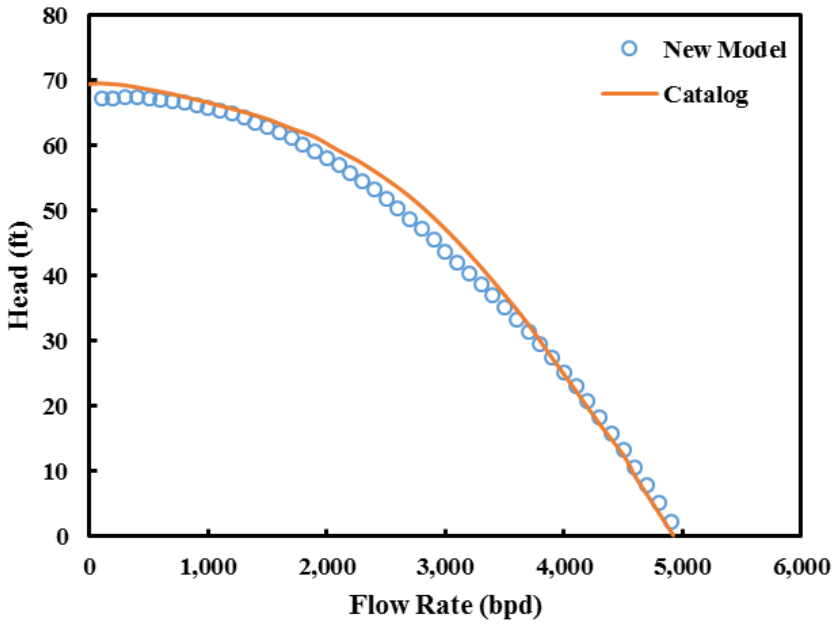

Figure 4.6 TE-2700 ESP Water Head Comparison of New Model and Catalog

4.2.2 GC-6100 ESP Setup

GC-6100 ESP is a mixed flow pump with a specific speed of 3,448. The geometrical parameters of GC-6100 ESP are the inputs of the mechanistic model.

The new model is also adapted to match the catalog water head curve by finding the flow rate at the BMP, which is 9,500 bpd. The water head predicted by this mechanistic model matches the catalog water head performance curve as well.

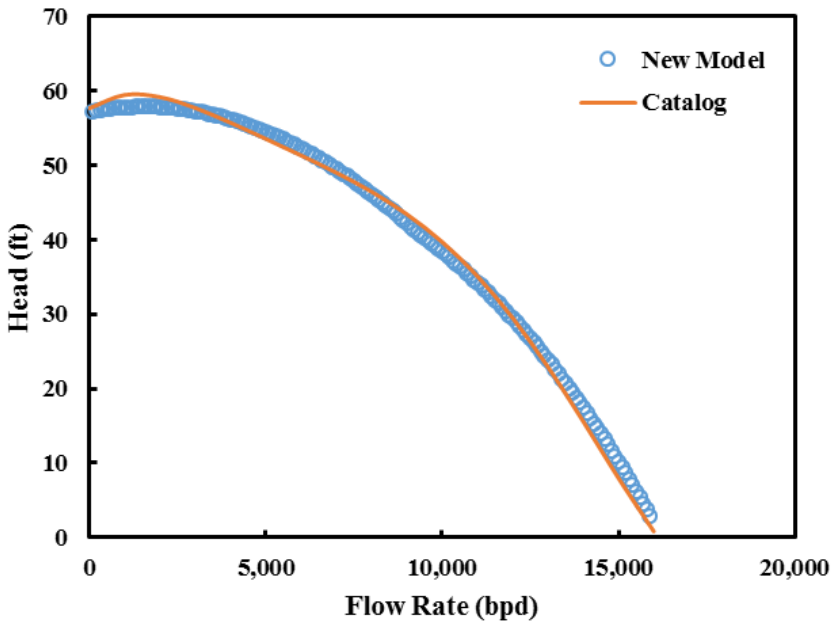

Figure 4.7 GC-6100 ESP Water Head Comparison of New Model and Catalog

4.3 Mechanistic Modeling Results

This section presents the mechanistic model validations by experimental data of TE-2700 ESP and GC-6100 ESP.

4.3.1 TE-2700 ESP Validation

The mechanistic model predictions are compared with TE-2700 ESP experimental results at 2,400 and 3,500 rpm. Figure 4.8 shows that the mechanistic model predicted water head matches the measured result.

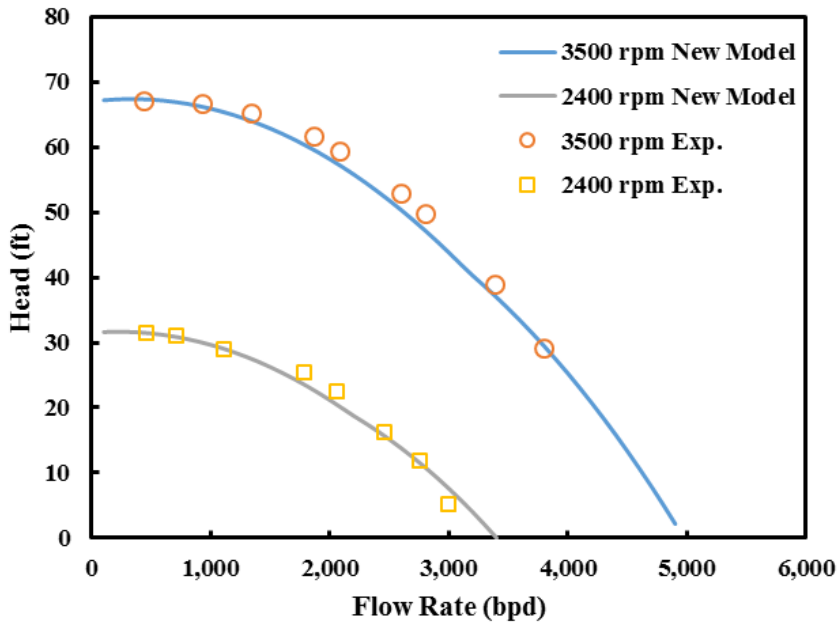

Figure 4.8 TE-2700 ESP Water Head Comparison of New Model and Experimental Data

Figure 4.9 shows the head comparison of this mechanistic model prediction and experiment data at 2,400 rpm under viscous fluid flow conditions and Figure 4.10 shows the comparison at 3,500 rpm. The mechanistic model prediction in terms of the head has a good agreement in the middle flow range.

In the mechanistic model, the same flow rate and fluid viscosity according to the experimental conditions are applied to calculate the head. Figure 4.11 summarizes the comparison results, which shows that the prediction errors are mostly bounded by ±10% error lines.

The Hydraulic Institute correction factors are also employed to predict the TE-2700 ESP hydraulic head under viscous fluid flow conditions. The hydraulic heads predicted by Hydraulic

Institute at 2,400 and 3,500 rpm are always higher than the experimental results as shown in Figure 4.12 and Figure 4.13 respectively, which means Hydraulic Institute correction factors do not work for TE-2700 ESP.

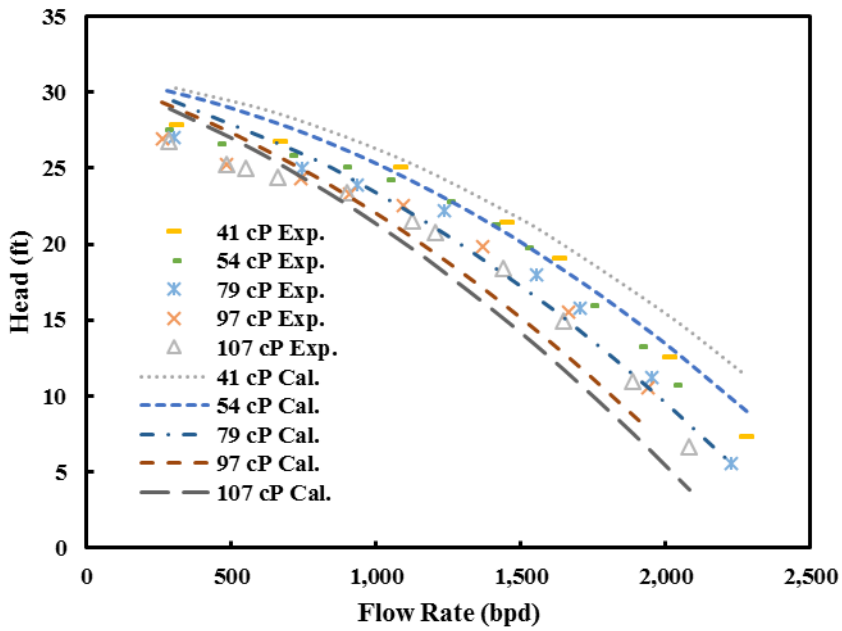

Figure 4.9 TE-2700 ESP Head Comparison of New Model and Experimental Data at 2,400 rpm

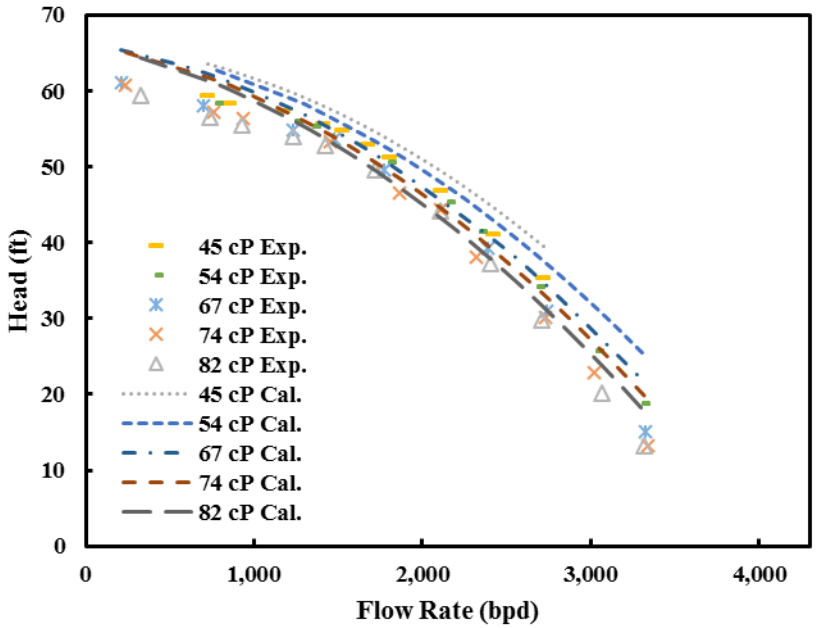

Figure 4.10 TE-2700 ESP Head Comparison of New Model and Experimental Data at 3,500 rpm

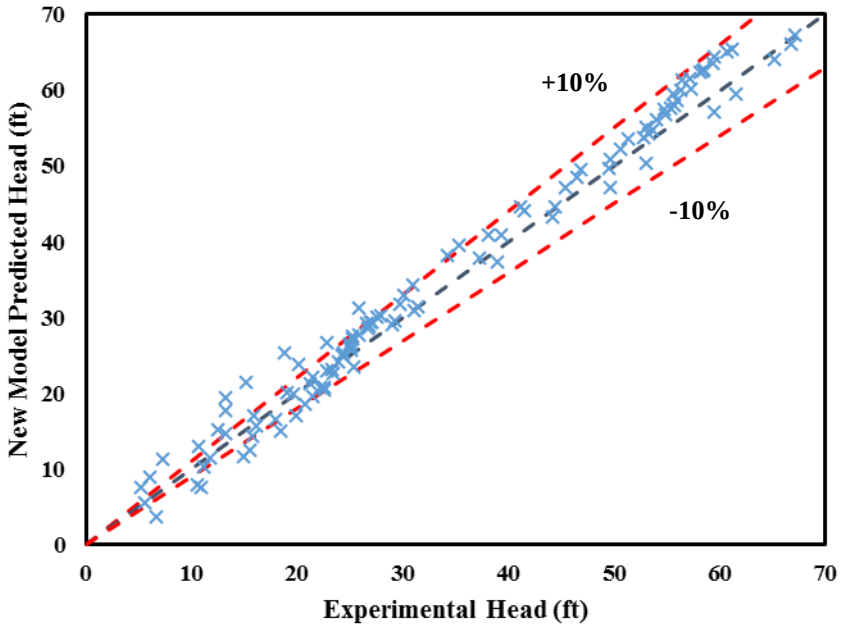

Figure 4.11 TE-2700 ESP Comparison of Model Predictions and Experimental Data

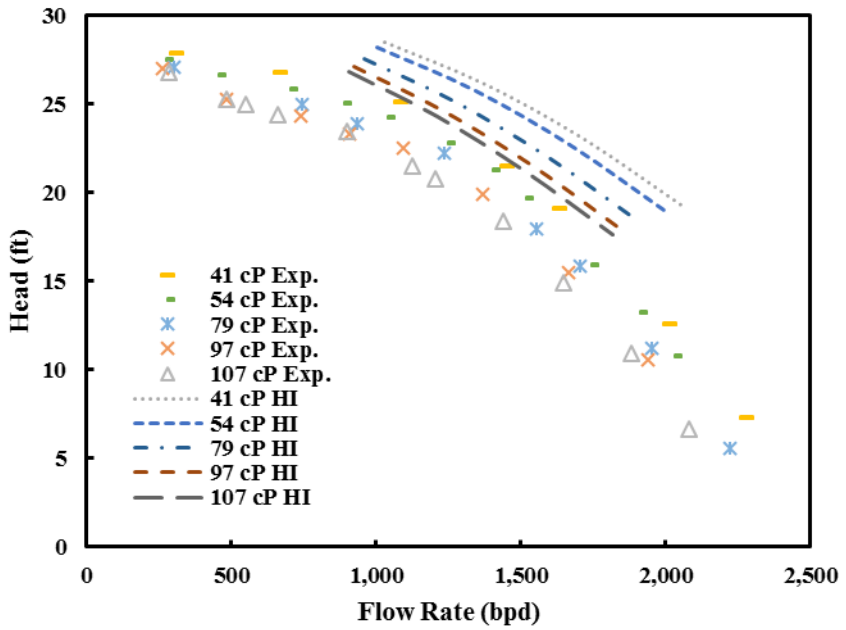

Figure 4.12 TE-2700 ESP Comparison of Hydraulic Institute Correction Factors Predictions and Experimental Data at 2,400 rpm

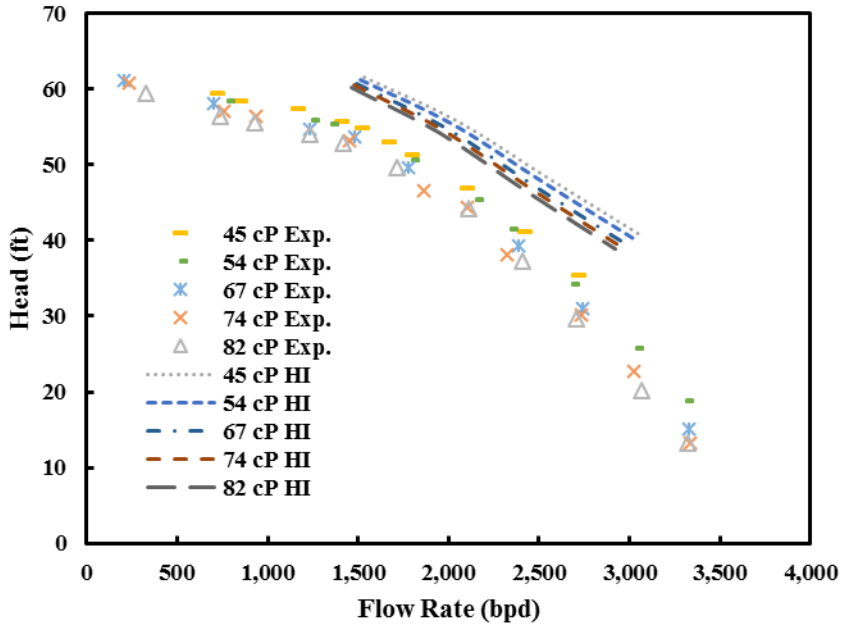

Figure 4.13 TE-2700 ESP Comparison of Hydraulic Institute Correction Factors Predictions and Experimental Data at 3,500 rpm

4.3.2 GC-6100 ESP Validation

GC-6100 ESP water head from experiments is compared with the head calculated from this mechanistic model at 2,400, 3,000, and 3,600 rpm as shown in Figure 4.14. The predicted water head agrees with the experimental results at different rotational speeds.

GC-6100 ESP head with different fluid viscosities is compared between experimental results and the mechanistic model at 2,400, 3,000, and 3,600 rpm as shown in Figure 4.15, Figure 4.16, and Figure 4.17 respectively. The heads predicted by the mechanistic model are a little bit lower than the experimental data at 2,400 rpm in Figure 4.15. Figure 4.16 shows that the mechanistic model head predictions have a great agreement with the experimental results at 3,000 rpm. In Figure 4.17, the head predictions are a little bit higher than the experimental results in the middle flow rate range at 3,600 rpm. Overall, most predictions are within ±10% error as shown in Figure 4.18.

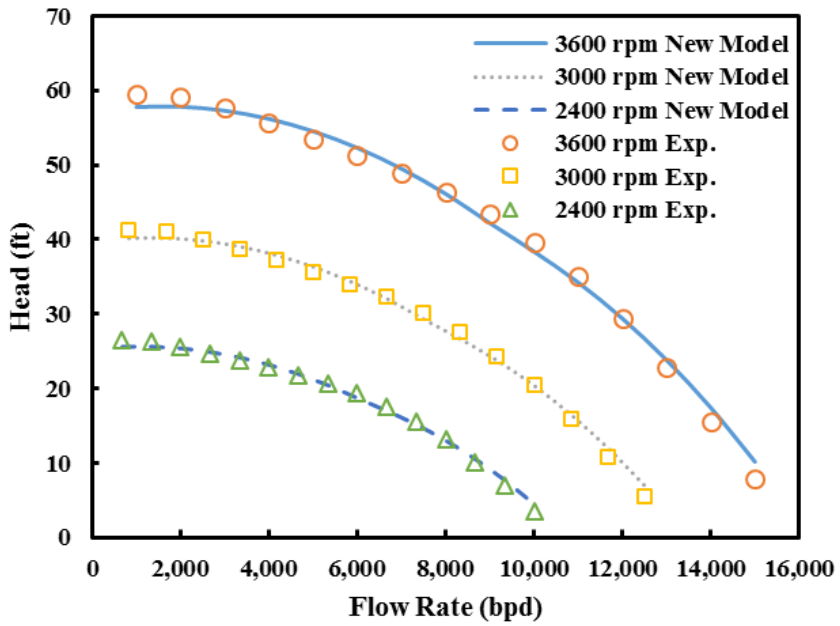

Figure 4.14 GC-6100 ESP Water Head Comparison of New Model and Experimental Data

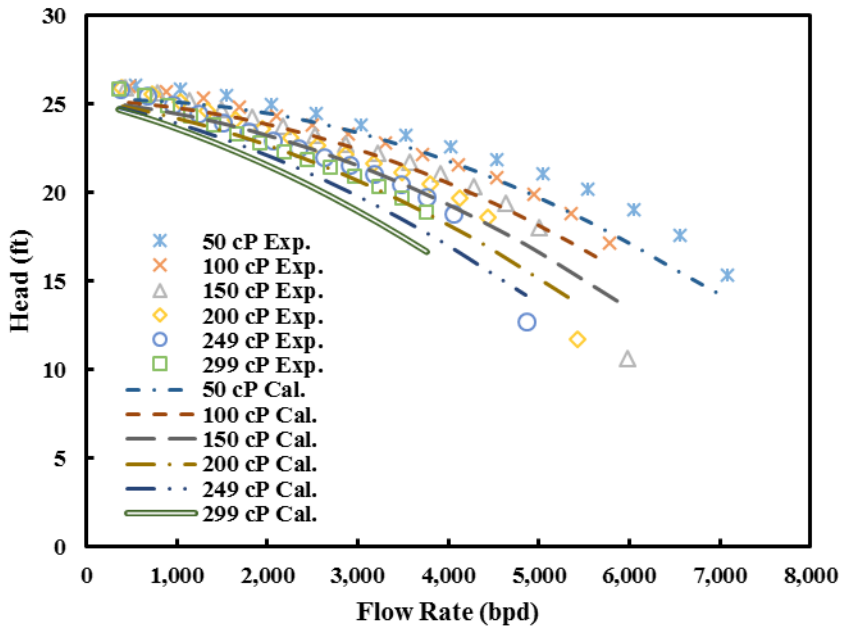

Figure 4.15 GC-6100 ESP Head Comparison of New Model and Experimental Data at 2,400 rpm

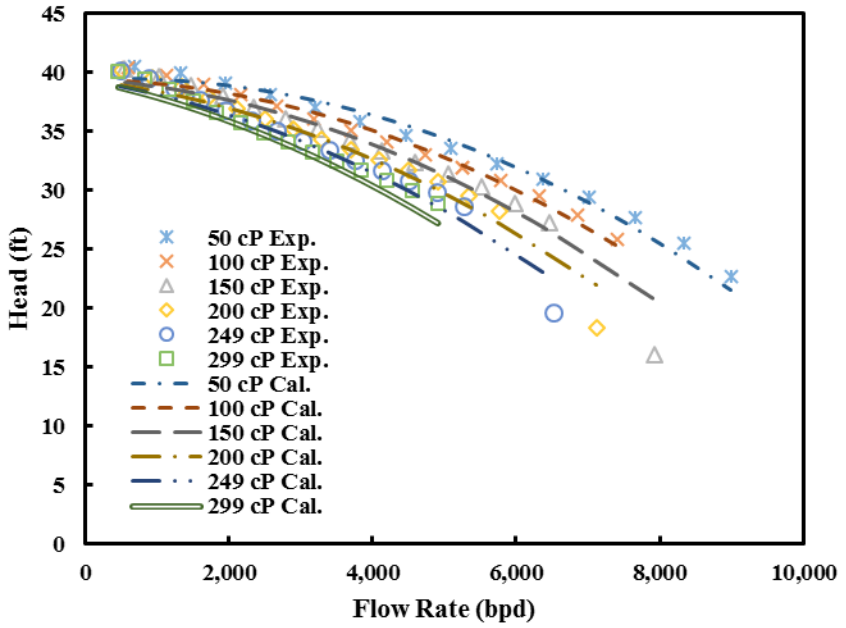

Figure 4.16 GC-6100 ESP Head Comparison of New Model and Experimental Data at 3,000 rpm

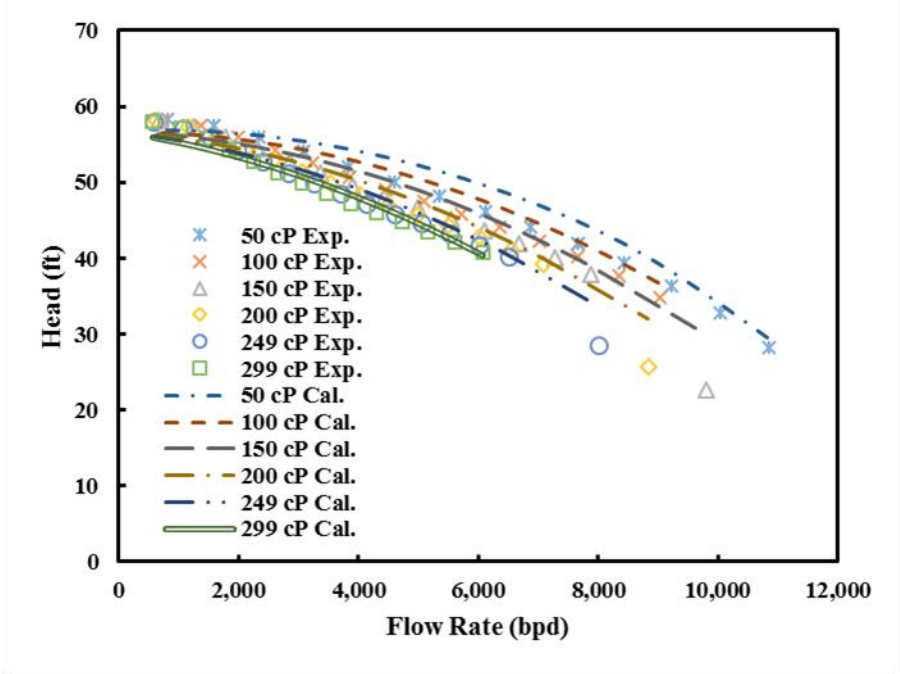

Figure 4.17 GC-6100 ESP Head Comparison of New Model and Experimental Data at 3,600 rpm

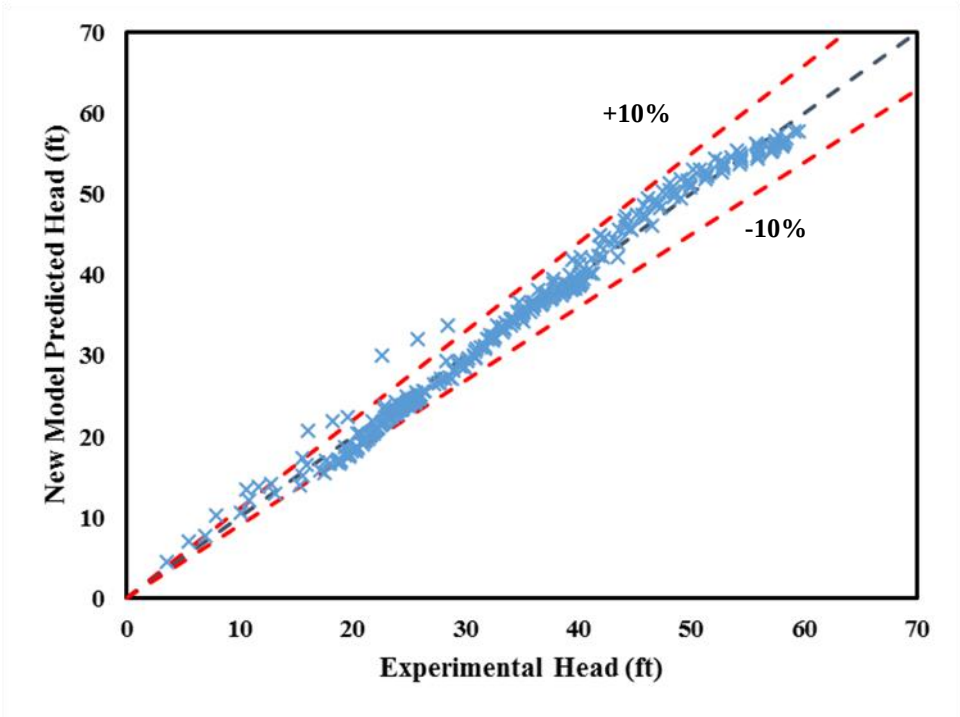

Figure 4.18 GC-6100 ESP Comparison of Model Predictions and Experimental Data

The Hydraulic Institute correction factors are used to predict the GC-6100 ESP hydraulic head with the same experimental oil viscosities as well. In Figure 4.19, the heads predicted by Hydraulic Institute correction factors are lower than the experimental data at 2,400 rpm. In Figure 4.20, the Hydraulic Institute correction factors prediction in terms of the head is relatively close to the experimental results at 3,000 rpm. The head prediction is always higher than the experimental results at 3,600 rpm as shown in Figure 4.21.

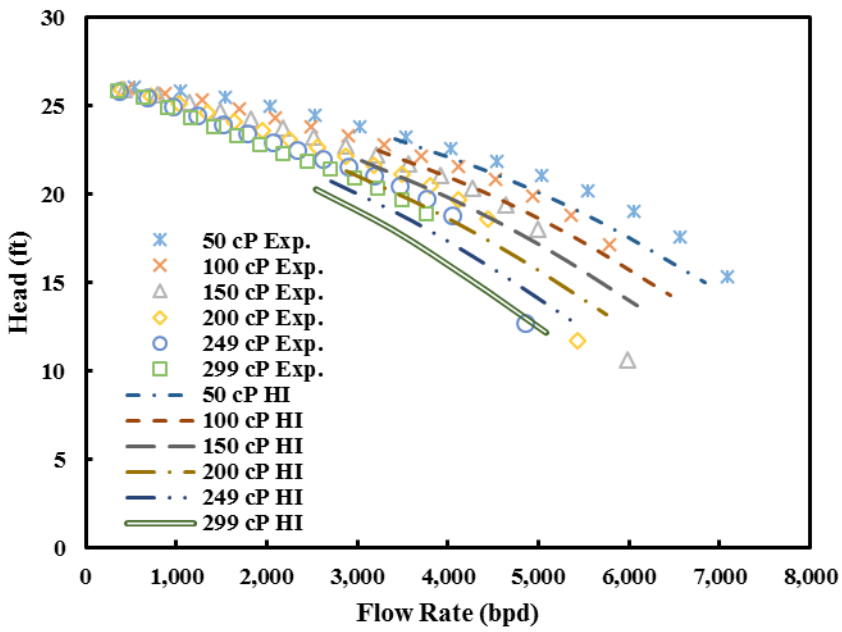

Figure 4.19 GC-6100 ESP Comparison of Hydraulic Institute Correction Factors Predictions and Experimental Data at 2,400 rpm

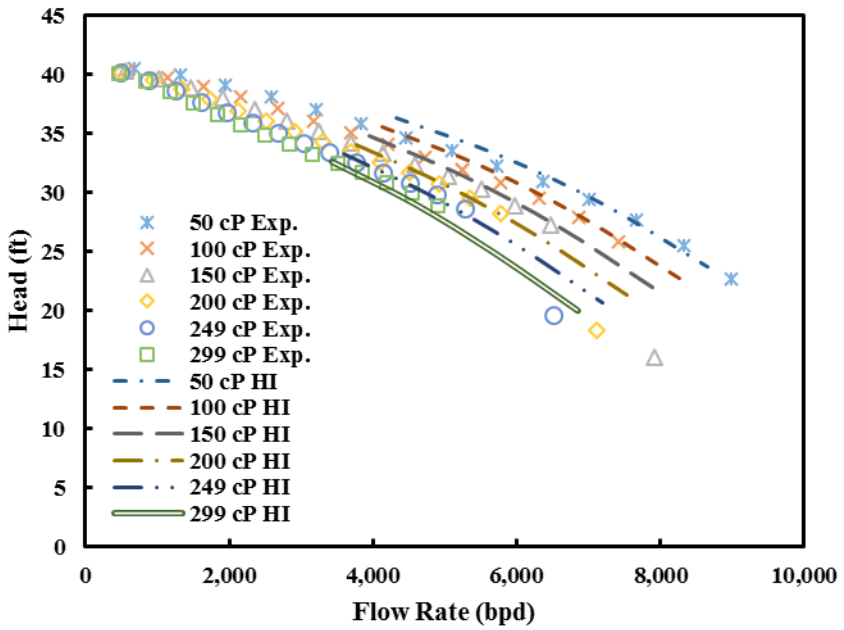

Figure 4.20 GC-6100 ESP Comparison of Hydraulic Institute Correction Factors Predictions and Experimental Data at 3,000 rpm

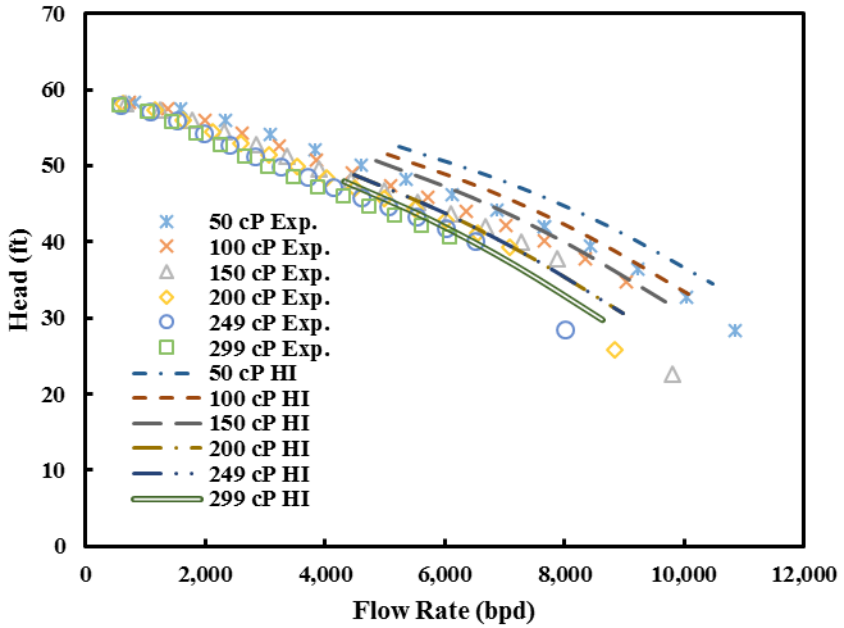

Figure 4.21 GC-6100 ESP Comparison of Hydraulic Institute Correction Factors Predictions and Experimental Data at 3,600 rpm

CHAPTER 5

CONCLUSIONS AND RECOMMENDATIONS

Three methods are used in this thesis, which are experiment, CFD simulation, and mechanistic modeling, to study the ESP performance under viscous fluid flow conditions.

5.1 Summary and Conclusions

5.1.1 Experimental Study

1. A closed flow loop is built and a data acquisition system is setup to measure the ESP boosting pressure with tap water and viscous oil. The measured water heads of TE-2700 ESP at 2,400, 3,000, and 3,500 rpm match the catalog water head curves. The measured brake horsepower (BHP) matches the average catalog BHP.
2. TE-2700 ESP is tested with ND20 at two rotational speeds of 2,400 and 3,500 rpm. The fluid viscosity is measured by the pipe viscometer and is controlled by changing the fluid temperature using a pipe-in-pipe heat exchanger. In laminar flows, the pressure drop measured over pipe viscometer is proportional to the flow rate, which validates the pipe viscometer. At 2,400 rpm, the oil viscosity increases from 41 to 107 cP. At 3,500 rpm, the fluid viscosity ranges from 45 to 85 cP.
3. The ESP head deteriorates as the oil viscosity increases. The ESP head at the low flow rate is less influenced by viscous effect. However, the fluid viscosity affects pump boosting pressure more at the high flow rate.

5.1.2 CFD Simulation

1. Three-dimensional CFD simulation is conducted before the experimental tests to simulate viscous effects on ESP performance and help optimize flow loop design. The predicted water head of TE-2700 ESP at 3,500 rpm matches the catalog water head curve, which verifies the CFD setup. The BHP predicted by CFD is lower than the catalog at the low flow rate but higher at the high flow rate. It can be concluded that CFD is better to predict hydraulic heads.
2. TE-2700 ESP is simulated by CFD with fluid viscosities from 1 to 1,000 cP. ESP becomes inefficient as the fluid viscosity becomes too high. The ESP head curve turns linear against liquid flow rate with flow regime transition from turbulent to laminar.
3. Compared with experimental results, CFD simulation underestimates the fluid viscosity effect on TE-2700 ESP. The simplification of fluid domains and CFD setup may results in this underestimation.

5.1.3 Mechanistic Modeling

1. A mechanistic model for ESP hydraulic head prediction is developed. The flow rate at the best match point (BMP) is applied to calculate the effective velocity at the ESP impeller outlet. The head losses including friction losses, turn losses, and leakage losses are also considered in the model. Therefore, the effect of fluid viscosity on ESP hydraulic head is included.
2. The hydraulic head predicted by the mechanistic model is compared with TE-2700 ESP measured head in this study and GC-6100 ESP experimental data. The mechanistic model is validated with the prediction error within ±10%.

5.2 Recommendations

1. More experimental data can be collected with higher viscosity fluid and different types of ESP so that the mechanistic model can be verified with wider experimental results.
2. A boosting pump is recommended to measure the ESP performance for the full flow rate range.
3. A torque sensor with a smaller measurement range is needed to measure the torque accurately. Or the electric power driving the motor is measured to estimate the BHP. Therefore, the pump power and efficiency can be studied under viscous fluid flow conditions.
4. The flow rate cannot be controlled precisely due to the wear condition of the pneumatic control value. A new pneumatic control valve is recommended.
5. In this thesis, all the tests are conducted in the fall and winter. It is better to put insulations on the water tank and the pipe-in-pipe heat exchanger if the experiment is conducted during the summer. Also, a sufficient amount of ice should be put into the water tank for the temperature control.

NOMENCLATURE

A	area, L^2, m^2
ΔP	differential pressure, $M/(LT^2)$, Pa
BEP	best efficiency point
BHP	brake horsepower, ML^2/T^3, $kg \cdot m^2/s^3$
BMP	best match point
C	absolute velocity, L/T, m/s
f	friction factor
H	hydraulic head, L, m
L	channel length, L, m
n	rotational speed, 1/T, rpm
N	rotational speed, rpm, 1/T, rpm
p	pressure, $M/(LT^2)$, Pa
P	pressure, $M/(LT^2)$, Pa
Q	flow rate, L^3/T, m^3/s
R	radius, L, m
Re	Reynolds number
T	blade thickness, L, m
T	torque, $(ML^2)/T^2$, $kg \cdot m^2/s^2$
U	peripheral velocity, L/T, m/s

V	velocity, L/T, m/s
W	relative velocity in ESP, L/T, m/s
y	channel height, L, m
Z	number

Greek Symbols

β	tangential blade angle, °
η	efficiency
ν	kinematic viscosity, L^2/T, m^2/s
μ	dynamic viscosity, M/(LT), Pa·s
ρ	fluid density, M/L^3, kg/m^3
σ	slip coefficient or velocity reduction factor

Subscripts

1	inlet
2	outlet
B	impeller blade
bep	best efficiency point
BEP	best efficiency point
BMP	best match point
D	diffuser
E	Euler
EE	effective Euler

H	head
Q	flow rate
s	slip or specific
V	diffuser vane
w	water

Superscripts

vis	viscous fluid
water	water

BIBLIOGRAPHY

1. Amaral, G., Estevam, V., and França, F.A., 2009. On the influence of viscosity on ESP performance. SPE *Production & Operations*. 24 (2): 303-310.
2. Amaral, G.D.L., 2007. Single-phase flow modeling of an ESP operating with viscous fluids. M.Sc. Thesis, State University of Campinas, Campinas, São Paulo, Brazil.
3. Banjar, H.M., Gamboa, J., Zhang, H.-Q., 2013. Experimental study of liquid viscosity effect on two-phase stage performance of electrical submersible pumps. SPE Annual Technical Conference and Exhibition, Society of Petroleum Engineers, New Orleans, Louisiana, September, 2013.
4. Barrios, L.J., Scott, S.L., Sheth, K.K., 2012. ESP technology maturation: subsea boosting system with high GOR and viscous fluid. SPE Annual Technical Conference and Exhibition, Society of Petroleum Engineers, San Antonio, Texas, October, 2012.
5. Bing, H., Tan, L., Cao, S.L., Lu, L., 2012. Prediction method of impeller performance and analysis of loss mechanism for mixed-flow pump. Sci. China Technol. Sci. 55(7), 1988–1998(p).
6. Churchill, S.W., 1977. Friction-factor equation spans all fluid-flow regimes. *Chemical engineering*, 84(24): 91-92.
7. Euler, L., 1752. Maximes pour arranger le plus avantageusement les machines destinées à élever de l'eau par moyen des pompes (Maxims for arranging most advantageously machines intended to raise water by means of pumps), *Mémoires de l'Académie Royale des Sciences et des Belles Lettres à Berlin*, 8: 185-232.

8. Euler, L., 1754. Théorie plus complette des machines qui sont mises en mouvement par la réaction de l'eau (More complete theory of machines that are set in motion by reaction with water), *Mémoires de l'Académie Royale des Sciences et des Belles Lettres à Berlin*, 10: 227-295.

9. Gamboa, J., and Prado, M., 2011. Review of electrical-submersible-pump surging correlation and models. SPE *Production & Operations*, 26(04): 314-324.

10. Gülich, J.F., 1999a. Pumping highly viscous fluids with centrifugal pumps – Part 1. World Pumps 1999a (395), 30–34.

11. Gülich, J.F., 1999b. Pumping highly viscous fluids with centrifugal pumps – Part 2. World Pumps 1999b (396), 39–42.

12. Gulich, J.F., 2007. *Centrifugal Pumps*. Berlin Heidelberg, Springer, New York.

13. Hinze, J.O., 1955. Fundamentals of the hydrodynamic mechanism of splitting in dispersion processes. AIChE *Journal*, 1(3): 289-295.

14. Hole, G., 1994. Fluid Viscosity Effects on Centrifugal Pumps. Pumps and Systems Magazine, April, 1994.

15. Hydraulic Institute, 1948. Tentative Standards of Hydraulic Institute: Charts for the Determination of Pump Performance When Handling Viscous Liquids. The Institute, OH.

16. Ippen, A.T., 1945. The Influence of Viscosity on Centrifugal Pump Performance. Issue 199 of Fritz Engineering Laboratory Report, ASME Paper No. A-45-57.

17. Kirby, B.J., 2010. *Micro- and Nanoscale Fluid Mechanics: Transport in Microfluidic Devgices.* Cambridge University Press.

18. Li, W.G., 2000. The “sudden-rising head” effect in centrifugal oil pumps. *World Pumps*, 2000(409): 34-36.

19. Li, W.G., 2002. Experimental investigation of performance of commercial centrifugal oil pump. World Pumps 2002 (425), 26–28.

20. Monte Verde, W., Biazussi, J., Bannwart, A., Arrifano Sassim, N., Estevam, V., 2013. Gas and Viscous Effects on the ESPs Performance. SPE Artificial Lift Conference-Americas, Society of Petroleum Engineers, Cartagena, Colombia, May, 2013.

21. Shojaeefard, M.H., Boyaghchi, F.A., Ehghaghi, M.B., 2006. Experimental study and three-dimensional numerical flow simulation in a centrifugal pump when handling viscous fluids. IUST *International Journal of Engineering Science*, 17 (3), 53–60.

22. Shojaeefard, M.H., Tahani, M., Ehghaghi, M.B., Fallahian, M.A., Beglari, M., 2012. Numerical study of the effects of some geometric characteristics of a centrifugal pump impeller that pumps a viscous fluid. *Computers & Fluids*, 2012 (60), 61–70.

23. Sirino, T., Stel, H., Morales, R.E., 2013. Numerical study of the influence of viscosity on the performance of an electrical submersible pump. ASME 2013 Fluids Engineering Division Summer Meeting, American Society of Mechanical Engineers, Incline Village, Nevada, July, 2013.

24. Solano, E.A., 2009. Viscous effects on the performance of electro submersible pumps (ESP's). Master’s Thesis, the University of Tulsa, Tulsa, OK.

25. Stel, H., Sirino, T., Ponce, F.J., Chiva, S., Morales, R.E.M., 2015. Numerical investigation of the flow in a multistage electric submersible pump. *Journal of Petroleum Science and Engineering*, 136: 41–54.

26. Stel, H., Sirino, T., Prohmann, P.R., Ponce, F., Chiva, S., Morales, R.E., 2014. CFD investigation of the effect of viscosity on a three-stage electric submersible pump. ASME 2014 4th Joint US-European Fluids Engineering Division Summer Meeting collocated with

the ASME 2014 12th International Conference on Nanochannels, Microchannels, and Minichannels. American Society of Mechanical Engineers, Chicago, Illinois, August, 2014.

27. Stepanoff, A.J., 1957. *Centrifugal and Axial Flow Pumps: Theory, Design and Application, 2nd Edition*. New York, NY, USA: John Wiley & Sons.

28. Sun, D. and Prado, M.G., 2006. Single-phase model for electric submersible pump (ESP) head performance. SPE *Journal*, 11(01): 80-88.

29. Trevisan, F., Prado, M., 2011. Experimental investigation of the viscous effect on two-phase-flow patterns and hydraulic performance of electrical submersible pumps. *Journal of Canadian Petroleum Technology*. 50 (4): 45–52.

30. Vieira, T.S., Siqueira, J.R., Bueno, A.D., Morales, R.E.M., and Estevam, V., 2015. Analytical study of pressure losses and fluid viscosity effects on pump performance during monophase flow inside an ESP stage. *Journal of Petroleum Science and Engineering*, 127(2015): 245-258.

31. White, F., 2005. *Viscous Fluid Flow, 3rd edition*. McGraw-Hill Series in Mechanical Engineering, McGraw-Hill Science.

32. Wiesner, F.J., 1967. A review of slip factors off centrifugal impeller. *J. Eng. Power*, 89(4), 558-566.

33. Wood Group ESP, 2004. *Product Catalog*. Wood Group ESP, Inc, Oklahoma City, OK.

34. Zhang, H.-Q., 2013. TUALP Spring Advisory Board Meeting, the University of Tulsa, Tulsa, OK.

35. Zhu, J., and Zhang, H.-Q., 2014. CFD simulation of ESP performance and bubble size estimation under gassy conditions. SPE Annual Technical Conference and Exhibition, Society of Petroleum Engineers, Amsterdam, the Netherlands, October, 2014.

36. Zhu, J., and Zhang, H.-Q., 2016. Mechanistic modeling and numerical simulation of in-situ gas void fraction inside ESP impeller. *Journal of Natural Gas Science and Engineering*, 36, 144-154.

37. Zhu, J., and Zhang, H.-Q., 2017. Modeling of gas bubble size in electrical submersible pump (ESP) through numerical simulation. SPE *Production & Operations*, 2017.

38. Zhu, J., Banjar, H., Xia, Z., and Zhang, H.-Q., 2016. CFD simulation and experimental study of oil viscosity effect on multi-stage electrical submersible pump (ESP) performance. *Journal of Petroleum Science and Engineering*, 146, 735-745.

39. Zhu, J., Guo, X., Liang, F., and Zhang, H.-Q., 2017. Experimental study and mechanistic modeling of pressure surging in electrical submersible pump. *Journal of Natural Gas Science and Engineering*, *45*: 625-636.

40. Zhu, J., 2017. Experiments, CFD simulation and mechanistic modeling of ESP performance under gassy conditions. Doctoral Dissertation, the University of Tulsa, Tulsa, OK.

APPENDIX A

EQUIPMENT AND INSTRUMENT SPECIFICATIONS

Table A.1 TUALP High-Viscosity ESP Flow Loop Equipment Specifications

Equipment	Model	Capacity	Purpose
ESP Pump	GE Oil & Gas Wood Group TE-2700	BEP:2700 bpd, 3,500 rpm	Testing Bench
Electric Motor	North American H3650	50 hp	Drive Motor
Air compressor	Kaeser CSD60	186 cfm, 217 psi	Air Source
Air Pressure Regulator	Speedaire 4ZM22	300 psi Max Inlet Pressure, 150 psi Max Outlet Pressure	Air Pressure Regulation
Variable Speed Drive	Hitachi L300P	50 hp	Altering Rotational Speed
ESP Thrust Chamber	Schlumberger REDA NO.88AB1- LT	-	Thrust Bearing Box
Liquid Pneumatic Control Valve	Fisher Body ED Actuator 657 Positioner 582i	-	Liquid Flow Rate Control
Water Pump	Dayton Stainless Steel Centrifugal Pump 2ZWT9A	0.5 hp	Water Circulation
Water Tank	Value Brand T-0300-059	300 gal	Water Storage
Water Pneumatic Control Valve	Fisher Body V100 Actuator 1052 Positioner 3622	-	Water Flow Rate Control

Table A.2 TUALP High-Viscosity ESP Flow Loop Instrumentation Specifications

Instrument	Model	Range	Accuracy
Thermocouple	Thermo Electric TCMSC83077875	0 to 1600 °F	±0.75%
Resistance Temperature Detector	Omega PR-11-2-100-1/8-18-E	-200 to 600 °C	±0.15°C
Temperature Transmitter	INOR IPAQ R520	-	-

Absolute Pressure Transmitter	Emerson Rosemount 2051	0 to 500 psig	±0.1%
Differential Pressure Transmitter	Emerson Rosemount 3051S	-10 to 50 psig	±0.1%
Pipe Viscometer	Emerson Rosemount 3051S	-250 to 250 psig	±0.1%
Coriolis High Flow Rate Meter	Proline Promass 80E	0 to 6615 lb/min	Mass Flow: ±0.2% Volume Flow: ±0.2% Density: ±0.0005 g/cm^3
Coriolis Low Flow Rate Meter	Micro Motion CMF200	0 to 1600 lb/min	Mass Flow: ±0.1% Volume Flow: ±0.1% Density: ±0.0005 g/cm^3
Torque/Rotary Speed Sensor and Monitor	Sensor: Lebow model 1805 Monitor: Lebow model 7540	0 to 22000 rpm 0 to 5000 lb$_f$·in	±0.05%

Table A.3 TUALP High-Viscosity ESP Flow Loop DAQ Specifications

Device	**Features**
Data Processing Computer	Dell Optiplex 9020, i7-4770 CPU @ 3.4 GHz, RAM: 16GB, HD: 1TB
National Instruments cFP-AI-110	• Eight analog voltage or current input channels • Eight voltage input ranges: 0–1 V, 0–5 V, 0–10 V, ±60 mV, ±300 mV, ±1 V, ±5 V, and ±10 V • Three current input ranges: 0–20, 4–20, and ±20 mA • 16-bit resolution • Three filter settings: 50, 60, and 500 Hz • 250 V_{rms} CAT II continuous channel-to-ground isolation, verified by 2,300 V_{rms} dielectric withstand test • –40 to 70 °C operation • Hot swappable
National Instruments cFP-AI-111	• Sixteen single-ended analog current input channels • Three input ranges: ±20, 0–20, and 4–20 mA • 16-bit resolution • Three filter settings: 50, 60, and 500 Hz • Hot swappable • 2300 V_{rms} transient overvoltage protection • –40 to 70 °C operation
National Instruments cFP-AO-200	• Eight 0–20 or 4–20 mA outputs • 0.5 mA overranging • 12-bit resolution • Up to 1 kΩ load impedance (with 24 V loop supply) • Indicators for open current loops

	• Short-circuit protection • 2300 V_{rms} transient overvoltage protection between the inter-module communication bus and the I/O channels • –40 to 70 °C operation • Hot plug-and-play
National Instruments cFP-1804	• Network interface: 10 BaseT and 100 BaseTX Ethernet, IEEE802.3, 10/100 Mbps • One RS-232 (DCE) serial port, 300 to 115200 bps • 11 to 30 VDC, 20W • 2300 V_{rms} transient overvoltage protection • –40 to 70 °C operation
National Instruments cFP-CB-1	• cFP-CB-1 is designed for general-purpose and hazardous voltage1 operation with all Compact FieldPoint I/O modules • 36 terminals available • Tie-wrap anchors for wires • Color-coded V and C terminals for voltage supply and common connections • –40 to 70 °C operation

Table A.4 Coriolis Flow Meters Specifications

	High Flow Meter	**Low Flow Meter**
Model	Promass 80E	CMF200M
Brand	Endress+Hauser	Emerson
Meter Size (inch)	3	2
Accuracy	0.20%	0.25%
Accurate Measurement Range (bpd)	>1700	>150
Pressure Drop at 300cP (psi)	12.2 at 10,000 bpd	13.7 at 2,100 bpd
Pressure Drop at 700cP (psi)	18.8 at 10,000 bpd	25.6 at 2,100 bpd
Pressure Drop at 1000cP (psi)	23.0 at 10,000 bpd	34.1 at 2,100 bpd

Table A.5 Pipe-in-Pipe Heat Exchanger Design Data

	Hot Fluid	**Cold Fluid**
Heat Transfer Media	SAE 5W-30 engine oil	Water
Volume Flow Rate (bpd)	10000	1940
Inlet Temperature (°C)	35	0
Outlet Temperature (°C)	34.5	1

Density (kg/m^3)	855	1001
Specific Heat (W/K)	1878	4129
Viscosity (cP)	65.9	1.7
Thermal Conductivity (W/m·K)	0.138	0.570
Pressure Drop (psi)	0.35	0.00
Log Mean Temp Difference (°C)	34.25	
Heat Transfer Rate (BTU/hr)	50375	
Heat Transfer Area (ft^2)	21	
Length (ft)	27	

Figure A.1 Pipe Viscometer

Figure A.2 Coriolis Flow Meters

Figure A.3 Flow Rate Control

Figure A.4 Pipe-in-Pipe Heat Exchanger

Figure A.5 Water Circulation System

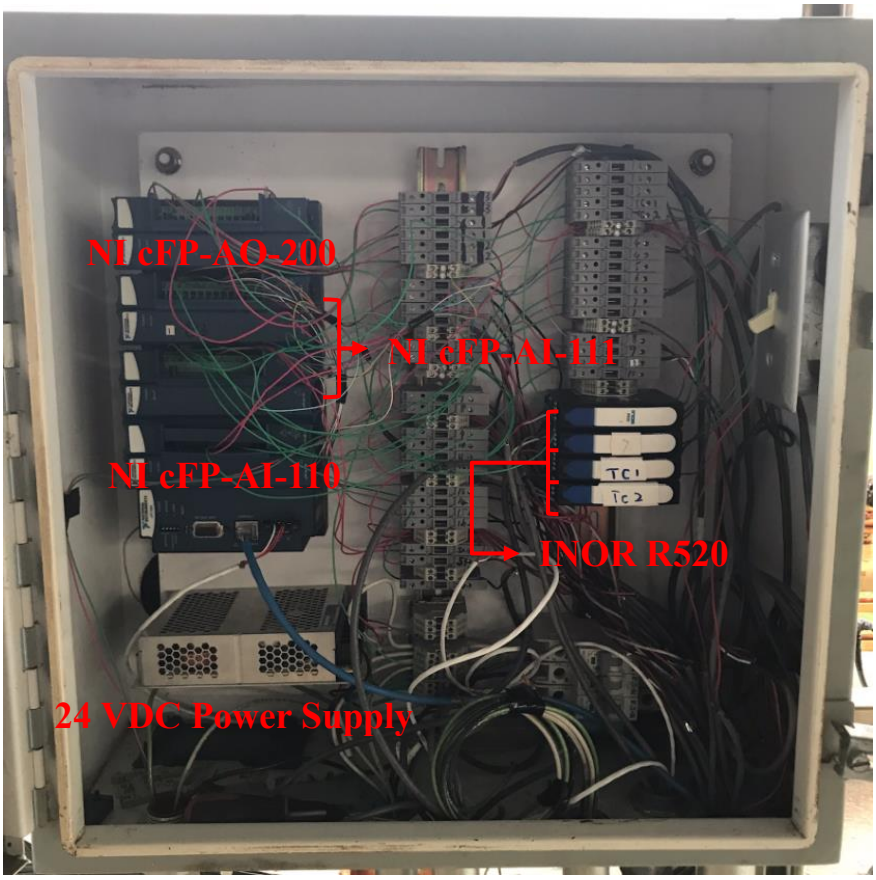

Figure A.6 Data Acquisition Devices

APPENDIX B

CHANNEL DISTRUBUTIONS OF NI MODULES

Table B.1 cFP-AI-110 Module #1 Channel Dsicturbutions

Channel	Description	Measurement Location
0	Torque	ESP Shaft
1	Rotational Speed	ESP Shaft
2	Not Used	
3	Not Used	
4	Not Used	
5	Not Used	
6	Not Used	
7	Not Used	

Table B.2 cFP-AI-111 Module #2 Channel Dsicturbutions

Channel	Description	Measurement Location
0	Differential Pressure	ESP Stage 6-7
1	Temperature	ESP Stage 14
2	Temperature	ESP Intake
3	Mass Flow Rate	Promass 80E
4	Fluid Density	Promass 80E
5	Mass Flow Rate	CMF200M
6	Fluid Density	CMF200M
7	Differential Pressure	ESP Stage 4-14
8	Not Used	
9	Not Used	
10	Absolute Pressure	ESP Stage 2
11	Absolute Pressure	ESP Stage 3
12	Differential Pressure	ESP Stage 4-5
13	Differential Pressure	ESP Stage 5-6
14	Temperature	Water Tank
15	Temperature	The End of Pipe Viscometer

Table B.3 cFP-AI-111 Module #3 Channel Dsicturbutions

Channel	Description	Measurement Location
0	Differential Pressure	Pipe Viscometer
1	Absolute Pressure	ESP Stage 4
2	Absolute Pressure	ESP Stage 5
3	Absolute Pressure	ESP Stage 6
4	Absolute Pressure	ESP Stage 7
5	Absolute Pressure	ESP Stage 8
6	Absolute Pressure	ESP Stage 9
7	Absolute Pressure	ESP Stage 10
8	Absolute Pressure	ESP Stage 11
9	Absolute Pressure	ESP Stage 12
10	Absolute Pressure	ESP Intake
11	Differential Pressure	ESP Stage 1-2
12	Differential Pressure	ESP Stage 2-3
13	Differential Pressure	ESP Stage 3-4
14	Not Used	
15	Not Used	

Table B.4 cFP-AO-200 Module #4 Channel Dsicturbutions

Channel	Description
0	Liquid Control Valve
1	Variable Speed Drive
2	Water Control Valve
3	Not Used
4	Not Used
5	Not Used
6	Not Used
7	Not Used

APPENDIX C

VISCOSITY CALCULATION FROM PIPE VISCOMETER

The pressure drop in pipe flows is

$$\Delta P = f\frac{L}{D}\frac{\rho V^2}{2} \tag{C.1}$$

To calculate the viscosity, an initial fluid viscosity is guessed to determine the flow regime. The flow regime is determined by Reynolds number which is calculated by

$$Re = \frac{\rho V D}{\mu} \tag{C.2}$$

If it is laminar flow (*Re* <2100), a new Reynolds number is

$$Re = \frac{64}{f} \tag{C.3}$$

If it is turbulent flow, the Moody friction factor is

$$\frac{1}{\sqrt{f}} = -2.0log_{10}(\frac{\frac{\epsilon}{D}}{3.7} + \frac{2.51}{Re\sqrt{f}}) \tag{C.4}$$

A new Reynolds number is obtained by solving Eq. (C.4):

$$Re = \frac{2.51}{\sqrt{f}\left(10^{-\frac{1}{2\sqrt{f}}} - \frac{\frac{\epsilon}{D}}{3.7}\right)} \tag{C.5}$$

Therefore, a new Reynolds number is found either from laminar flow or from turbulent flow, then the viscosity is

$$\mu = \frac{\rho V D}{Re} \tag{C.6}$$

If the new viscosity is not close to the guessed viscosity, the new viscosity is treated as the guessed viscosity and the previous procedure is repeated until the relative error is in the tolerance. Figure C.1 shows the calculation procedure.

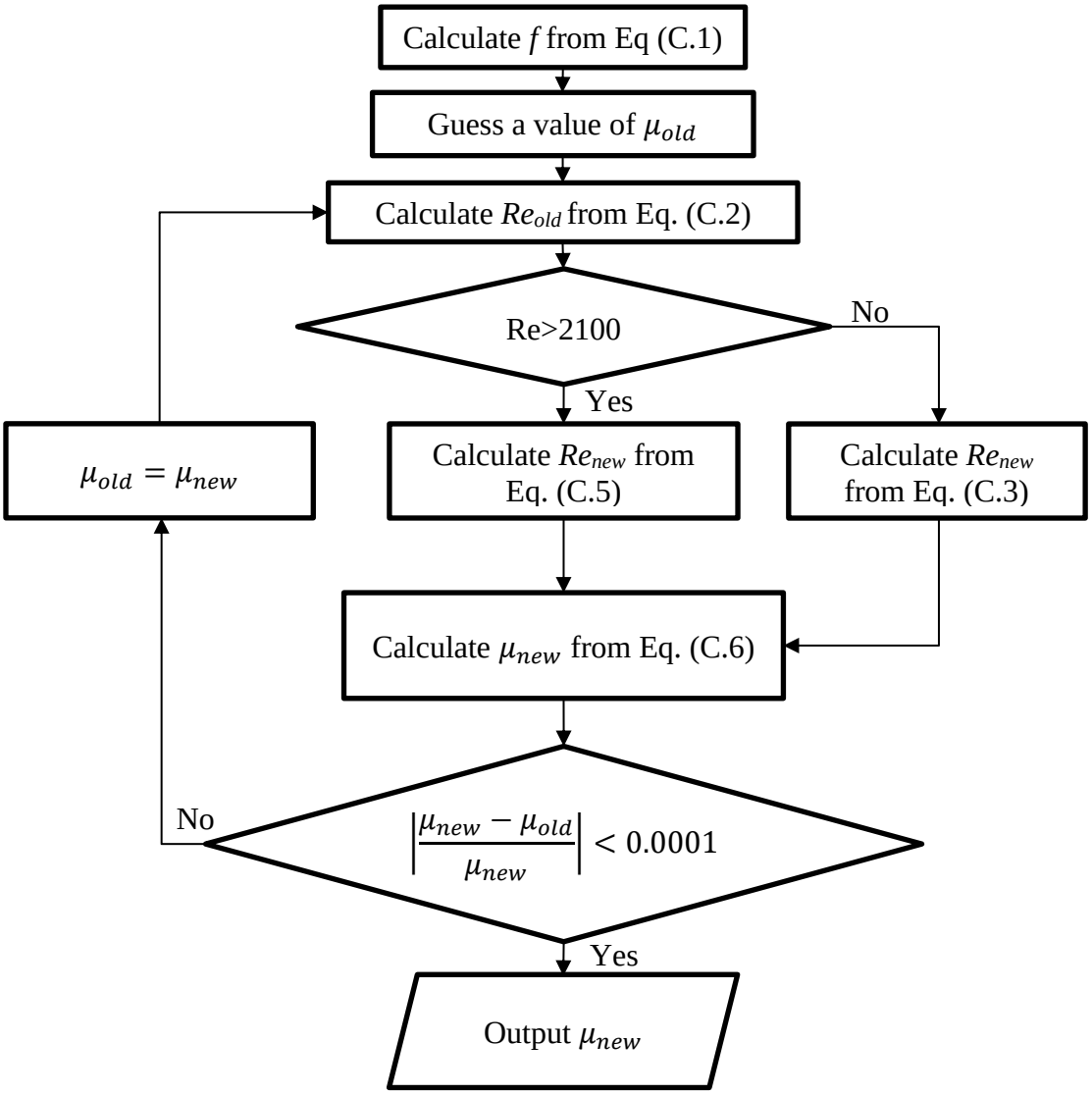

Figure C.1 Flow Chart for Viscosity Calculation from Pipe Viscometer

For high fluid viscosity tests, the flow regime is usually laminar and the pressure drop in pipe flows is

$$\Delta P = \frac{8\mu LQ}{\pi R^4} = \frac{128\mu LQ}{\pi D^4} \tag{C.7}$$

The viscosity is solved as

$$\mu = \frac{\Delta P \pi D^4}{128LQ} \tag{C.8}$$

The above equation can be written in English engineering units:

$$\mu\left(1000\frac{cP}{Pa\cdot s}\right) = \frac{\Delta P\left(\frac{1}{6894.76}\frac{psi}{Pa}\right)\pi D^4\left(39.3701\frac{inch}{m}\right)^4}{128L(3.28084\frac{ft}{m})Q(543\ 439.65\frac{bpd}{m^3/s})} \tag{C.9}$$

It is rearranged to write

$$\mu(cP) = 125582.5675\frac{\Delta P(psi)D^4(inch^4)}{L(ft)Q(bpd)} \tag{C.10}$$

The diameter of ASTM A312 Schedule 40 stainless 304/304L pipe is 3.068 inches so the above equation becomes

$$\mu(cP) = 11126300.34\frac{\Delta P(psi)}{L(ft)Q(bpd)} \tag{C.11}$$

For the 20-foot long pipe viscometer,

$$\mu(cP) = 556315\frac{\Delta P(psi)}{Q(bpd)} \tag{C.12}$$

For the 10-foot long pipe viscometer,

$$\mu(cP) = 1112630\frac{\Delta P(psi)}{Q(bpd)} \tag{C.13}$$

This method does not require initial guess viscosity and the viscosity can be found from the plot of the pressure drop over the pipe viscometer against the flow rate when the flow regime is laminar flow.

Figure C.2 shows the relationship between the DP over the pipe viscometer and the liquid

flow rate for different oil viscosities when testing TE-2700 ESP at 2,400 rpm. The linear fitting is presented, from which the oil viscosity can be obtained.

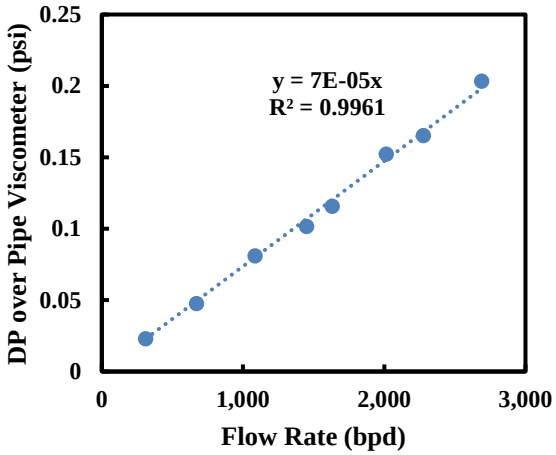

(a)

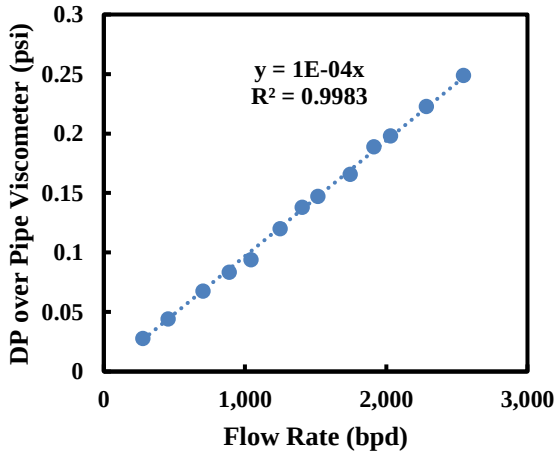

(b)

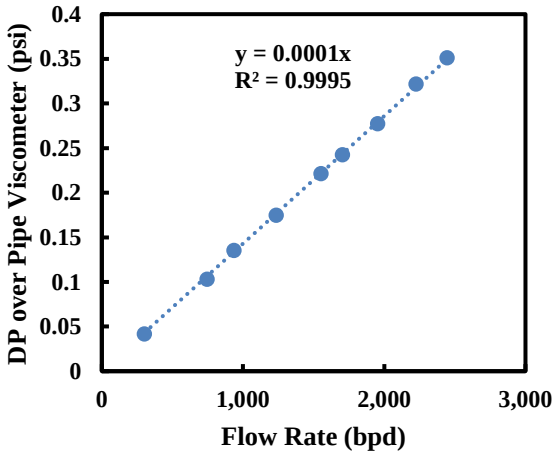

(c)

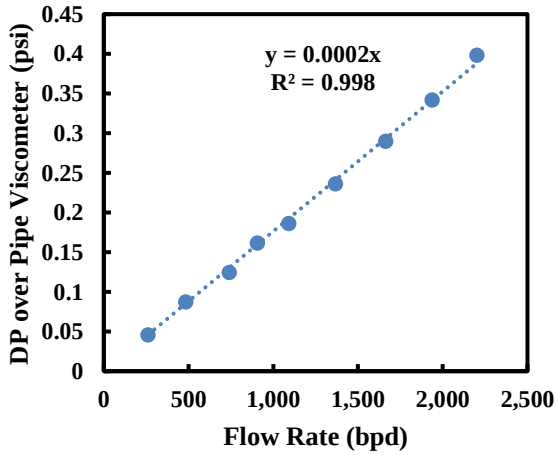

(d)

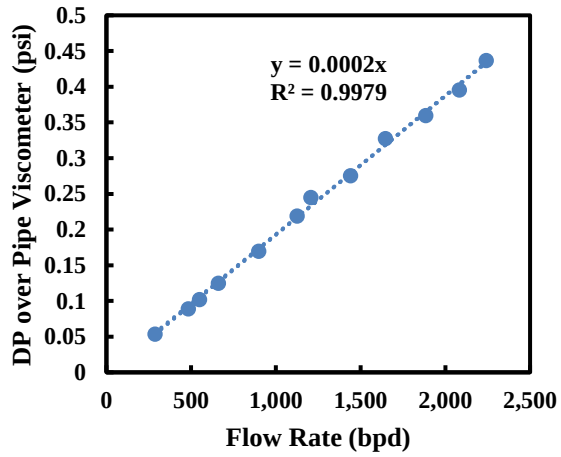

(e)

Figure C.2 Preesure Drop over Pipe Viscometer versus Flow Rate at (a) 41 cP, (b) 54 cP, (c) 79 cP, (d) 97 cP, and (e) 107 cP

Figure C.3 shows the relationship between the DP over the pipe viscometer and the liquid flow rate with changing fluid viscosities when testing TE-2700 ESP at 3,500 rpm, which also confirms the validity of pipe viscometer used for this study.

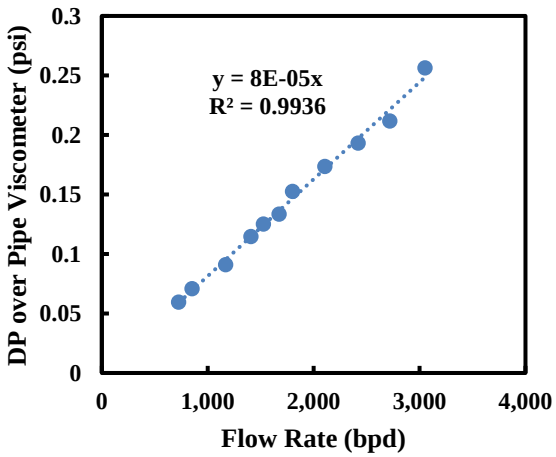

(a)

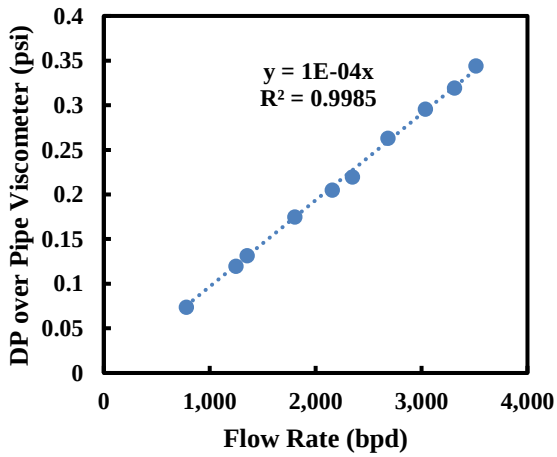

(b)

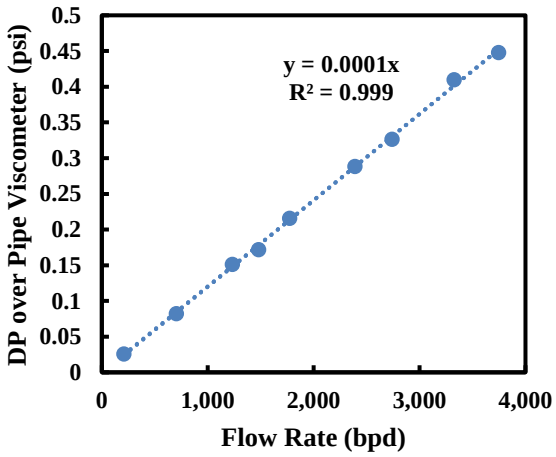

(c)

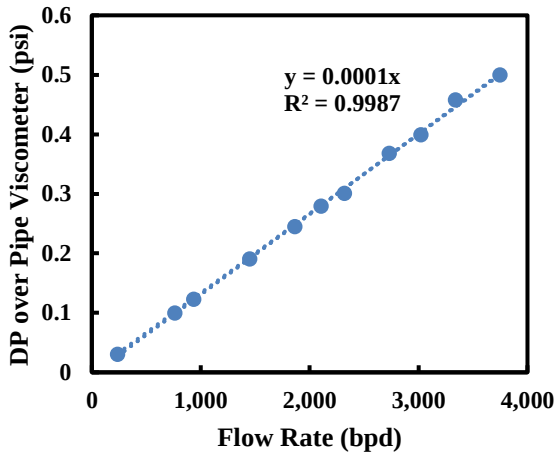

(d)

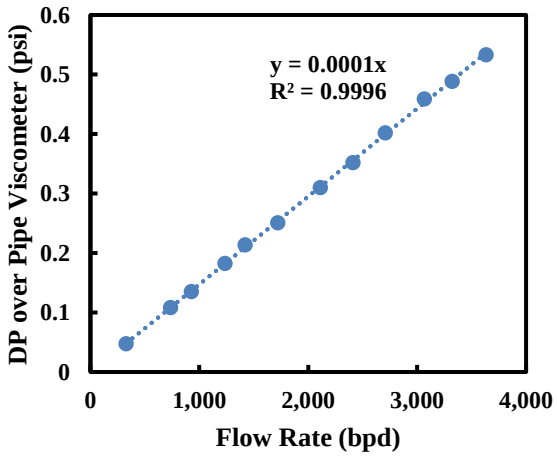

(e)

Figure C.3 Preesure Drop over Pipe Viscometer versus Flow Rate at (a) 45 cP, (b) 54 cP, (c) 67 cP, (d) 74 cP, and (e) 82 cP